Impact of global warming on the rise of volcanic plumes and implications for future volcanic aerosol forcing

Aubry, Thomas J.; Jellinek, A. Mark; Degruyter, Wim; Bonadonna, Costanza; Radić, Valentina; Clyne, Margot; Quainoo, Adjoa

How to cite

AUBRY, Thomas J. et al. Impact of global warming on the rise of volcanic plumes and implications for future volcanic aerosol forcing. In: Journal of geophysical research. Atmospheres, 2016, vol. 121. doi: 10.1002/2016JD025405

This publication URL: https://archive-ouverte.unige.ch/unige:90244
Publication DOI: 10.1002/2016JD025405

AGU PUBLICATIONS

JGR

Journal of Geophysical Research: Atmospheres

RESEARCH ARTICLE

10.1002/2016JD025405

Key Points:

- Projections of three GCMs imply that the maximum rise height of lowermost stratospheric volcanic plumes will decrease with global warming
- Decrease in plume height and increase in tropopause height will result in fewer stratopheric injections from volcanic eruptions
- Radiative forcing related to volcanic aerosol-radiation interactions is predicted to decline, in turn

Supporting Information:

- Supporting Information S1
- Figure S1
- Figure S2
- Figure S3

Correspondence to:
T. J. Aubry,
taubry@eoas.ubc.ca

Citation:
Aubry, T. J., A. M. Jellinek, W. Degruyter, C. Bonadonna, V. Radic, M. Clyne, and A. Quainoo (2016), Impact of global warming on the rise of volcanic plumes and implications for future volcanic aerosol forcing, *J. Geophys. Res. Atmos.*, *121*, doi:10.1002/2016JD025405.

Received 23 MAY 2016
Accepted 21 OCT 2016
Accepted article online 16 NOV 2016

Impact of global warming on the rise of volcanic plumes and implications for future volcanic aerosol forcing

Thomas J. Aubry[1], **A. Mark Jellinek**[1], **Wim Degruyter**[2], **Costanza Bonadonna**[3], **Valentina Radić**[1], **Margot Clyne**[1], and **Adjoa Quainoo**[1]

[1]Department of Earth, Ocean, and Atmospheric Sciences, University of British Columbia, Vancouver, British Columbia, Canada, [2]School of Earth and Ocean Sciences, Cardiff University, Cardiff, UK, [3]Department of Earth Sciences, University of Geneva, Geneva, Switzerland

Abstract Volcanic eruptions have a significant impact on climate when they inject sulfur gases into the stratosphere. The dynamics of eruption plumes is also affected by climate itself, as atmospheric stratification impacts plumes' height. We use an integral plume model to assess changes in volcanic plume maximum rise heights as a consequence of global warming, with atmospheric conditions from an ensemble of global climate models, using three representative concentration pathways (RCP) scenarios. Predicted changes in atmospheric temperature profiles decrease the heights of tropospheric and lowermost stratospheric volcanic plumes and increase the tropopause height, for the RCP4.5 and RCP8.5 scenarios in the coming three centuries. Consequently, the critical mass eruption rate required to cross the tropopause increases by up to a factor of 3 for tropical regions and up to 2 for high-latitude regions. A number of recent lower stratospheric plumes, mostly in the tropics (e.g., Merapi, 2010), would be expected to not cross the tropopause starting from the late 21st century, under RCP4.5 and RCP8.5 scenarios. This effect could result in a $\simeq$5–25% decrease in the average SO_2 flux into the stratosphere carried by small plumes, the frequency of which is larger than the rate of decay of volcanic stratospheric aerosol, and a $\simeq$2–12% decrease of the total flux. Our results suggest the existence of a positive feedback between climate and volcanic aerosol forcing. Such feedback may have minor implications for global warming rate but can prove to be important to understand the long-term evolution of volcanic atmospheric inputs.

1. Introduction

Explosive volcanic eruptions eject gases and ash into the atmosphere, which act to modify Earth's global radiative energy balance. At annual to centennial time scales, the injection of sulfur gases, resulting in the formation of sulfur aerosols, has the largest impact on Earth's radiative balance via scattering of Sun radiation and absorption of Sun and Earth radiation (aerosol-radiation interactions) [*Robock*, 2000; *Timmreck*, 2012]. Tropospheric volcanic aerosols are washed out within a few weeks. It is therefore commonly assumed that tropospheric aerosol-radiation interactions from individual eruptions are negligible at a global scale, although aerosol particles enhance cloud condensation nuclei and, thus, have an indirect impact via aerosol-cloud interactions on Earth's radiative balance [*Schmidt et al.*, 2012]. Stratospheric volcanic aerosols, by comparison, have a typical *e*-folding time of 1 year and exert a significant influence on climate over these time scales. These relatively long-lived particles scatter shortwave radiation and absorb longwave radiation, resulting in a net cooling of the troposphere and a net warming of the stratosphere [*Robock*, 2000; *Timmreck*, 2012]. In addition to these global effects on air temperature, stratospheric volcanic aerosol-radiation interactions can cause significant changes in atmospheric and oceanic circulation, sea ice dynamics [e.g., *Robock*, 2000; *Shindell et al.*, 2004; *Mignot et al.*, 2011; *McGregor and Timmermann*, 2010; *Driscoll et al.*, 2012; *Stoffel et al.*, 2015; *Toohey et al.*, 2016a], and precipitation patterns [e.g., *Iles and Hegerl*, 2015]. Whether an eruptive plume reaches the stratosphere also controls ozone depletion by halogen species injected by a volcano, although this forcing is small relative to aerosol-radiation interactions and largely depends on halogen scavenging in the plume [*Tabazadeh and Turco*, 1993; *Textor et al.*, 2003; *Timmreck*, 2012; *Carn et al.*, 2016].

In the context of present-day global warming, which is mostly driven by anthropogenic greenhouse gas emissions, volcanic aerosols are of particular importance because their atmospheric temperature fingerprint is opposed to the one of CO_2, i.e., a net warming of the troposphere and a net cooling of the stratosphere

[*Hartmann et al.*, 2013]. In particular, climate models neglecting aerosol-radiation interactions of stratospheric volcanic eruptions since 1998 are overestimating global warming, even though no major volcanic eruption occurred during this period [*Solomon et al.*, 2011; *Haywood et al.*, 2014; *Ridley et al.*, 2014; *Santer et al.*, 2014].

Critically, most projections from global climate models (GCMs) impose a constant volcanic radiative forcing [*Collins et al.*, 2013]. Only some decadal projection experiments assume that a Pinatubo-like eruption will occur at one given year to test sensitivity of short-term projections to volcanic eruptions [*Taylor et al.*, 2012]. Thus, GCMs are unable to predict temperature changes resulting from future eruptions, although their ability to simulate the climate response to past volcanic eruptions is continuously improved [*Timmreck*, 2012; *Flato et al.*, 2013]. Prediction of changes in future volcanic aerosol-radiation interaction would allow improved prediction of future climate.

There are two key controls on volcanic aerosol-radiation interactions resulting from a particular eruption: how much sulfur gas is expelled and whether this sulfur gas reaches the stratosphere.

Both controls partly depend on eruption source conditions and, in particular, on the mass eruption rate of the eruptive plume. The exact timing, global location, and source conditions of future eruptions are impossible to predict, which is a reason why most climate projections assume a constant volcanic radiative forcing. In addition, the height of a given volcanic plume H depends strongly on atmospheric stratification [*Morton et al.*, 1956; *Wilson et al.*, 1978; *Woods*, 2010]:

$$H \propto N^{-\kappa_1} M_0^{\kappa_2}\ , \tag{1}$$

where N is the Brunt-Väisälä frequency, M_0 is the mass eruption rate, $\kappa_1 = \frac{3}{4}$ and $\kappa_2 = \frac{1}{4}$ in the absence of wind [*Morton et al.*, 1956], and $\kappa_1 = \frac{2}{3}$ and $\kappa_2 = \frac{1}{3}$ under strong wind conditions [*Hewett et al.*, 1971]. The Brunt-Väisälä frequency mostly depends on the temperature lapse rate:

$$N^2 = \frac{g}{T}\left(\frac{g}{c_p} - \Gamma\right)\ , \tag{2}$$

where g is the Earth's gravitational acceleration, T is the atmospheric temperature, c_p is the air specific heat capacity, $\Gamma = -\frac{\mathrm{d}T}{\mathrm{d}z}$ is the lapse rate, and z is the altitude.

A major effect of present-day global warming is the decrease of the temperature lapse rate Γ in the tropical troposphere [e.g., *Simmons et al.*, 2014; *Sherwood and Nishant*, 2015] and, hence, an increase in the strength of the stratification which could result in a decrease of tropospheric plume height, in the tropics (equation (1)). The key question we ask in this paper is, thus, how will global warming impact the heights of plumes of future eruptions? In particular, will more or fewer eruptive plumes reach the stratosphere than at present, and how will it impact future volcanic aerosol-radiation interactions? Some of these questions are raised by *Glaze et al.* [2015] in the context of past climate change but have never been investigated into detail in the context of the present-day climate change. Understanding the climate change-driven controls on variations in volcanic plume height has fundamental implications also on the distribution of hazards associated with the dispersal and sedimentation of both lapilli-sized and ash-sized particles, e.g., from proximal damage to buildings and infrastructures to far-field risk to aviation and human health [*Rymer*, 2015].

Our paper is structured in the following way. Our methodology is described in detail in section 2: we use an integral volcanic plume model to predict changes in volcanic plume height driven by changes in atmospheric temperature, geopotential height, and wind fields inferred from GCM projections. In section 3, we show the impact of predicted changes of these fields on the plume height, as well as the impact of their combined effects. In section 4, we test the sensitivity of our results regarding the plume model parameterization and choice of GCM. Lastly, we estimate changes in the flux of volcanic SO_2 into the stratosphere driven by changes in plume height and discuss the implications of our results for future volcanic forcing.

2. Data and Plume Model

We apply an integral volcanic plume model to compute the height of explosive volcanic plumes. In each model run, we specify eruption source conditions and atmospheric conditions. We use atmospheric conditions associated with 12 active volcanic regions (Figure 1) over four different time intervals. The sample of 12 regions is chosen based on its large scatter both latitudinally and longitudinally, which facilitates the sensitivity test of our results to regional climate variability. The projections for atmospheric conditions are based on three

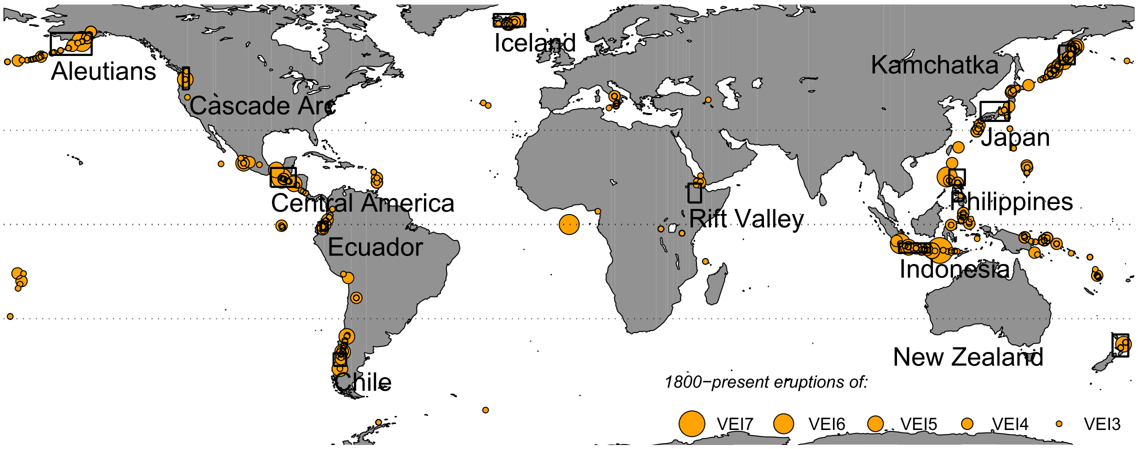

Figure 1. Global map with the 12 volcanically active regions selected for this study (black rectangles). Orange dots show large explosive eruptions (VEI of 3 to 7) for the last two centuries (from Global Volcanism Program database).

different greenhouse gas emission scenarios from an ensemble of three GCMs. Our overall methodology is summarized by the flow chart presented in Figure 2a, and the following sections provide more details on the data and integral volcanic plume model that are used.

2.1. Source Conditions

Source conditions that must be specified for each run of the integral volcanic plume model are the vent altitude and radius, the gas-ash mixture exit velocity, gas content, and temperature. We use two approaches to specify the source conditions of the model. First, we sample source conditions in a fixed parameter space (Table 1). A key source parameter controlling the height reached by a volcanic plume (equation (1)) is the mass eruption rate M_0:

$$M_0 = \pi \rho_0 R_0^2 U_0 \quad , \tag{3}$$

which is controlled by the vent radius R_0, the exit velocity U_0, and the bulk density of the ejected mixture ρ_0 which depends on the magma temperature and gas content. We will initially vary M_0 by considering variations in R_0 and U_0 only (section 3). The range in which we sample R_0 and U_0 is chosen to obtain mass eruption rates of $\simeq 10^6 - 10^8$ kg s^{-1}, which ensures that plume heights are between $\simeq$50 and 150% of the present-day

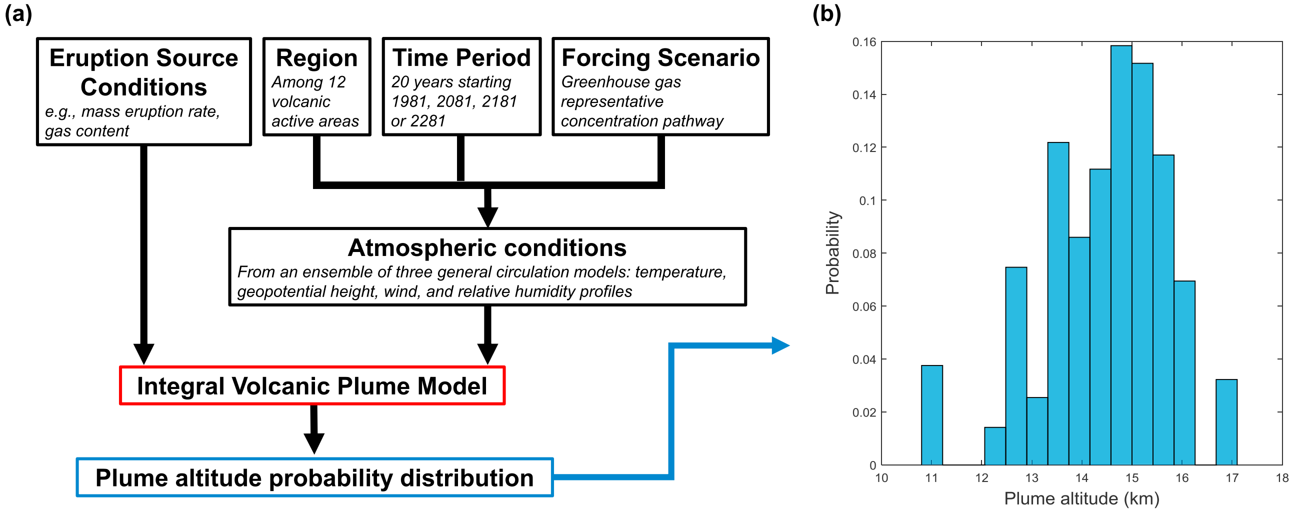

Figure 2. (a) Flow chart summarizing the methodology used. To compute the plume altitude probability distribution, we use an integral volcanic plume model. Eruption source conditions are sampled from a fixed parameter space. Atmospheric conditions depend on the chosen region, period, and greenhouse gas forcing (Representative Concentration Pathway). (b) Example of plume altitude probability distribution obtained for $M_0 = 3.7 \times 10^6$ kg s^{-1} in the Philippines, for the 1981–2000 period. The spread of the distribution is due to variability in temperature, geopotential height, and horizontal wind within the 20 year period.

Table 1. Values of Parameters Used in the Integral Volcanic Plume Model (Greek Symbols) and of Eruption Source Conditions (Symbols With Subscript 0)

Parameter	Symbol	Unit	Value	Range
Radial entrainment coefficient	α	-	0.1	0.07–0.13
Wind entrainment coefficient	β	-	0.7	0.35–1
Condensation rate	λ	s^{-1}	0	0–0.098
Temperature	T_0	K	1200	1000–1400
Gas mass fraction	n_0	-	0.04	0.01–0.07
Velocity	U_0	m s^{-1}	75–300	75–300
Vent radius	R_0	m	10–150	10–150
Vent height	H_0	m	1500	local topography[a]

[a] Vent height is sampled from a distribution representative of the altitude of volcanoes in the region considered (cf. supporting information Text S4) or from the *Carn et al.* [2016] data set.

tropopause height. We return to the sensitivity of our results to natural variability in other source parameters, including the vent altitude, in section 4.

Next, we use the data set of *Carn et al.* [2016] to test the model using source conditions inferred for historical eruptions. We use this data set because it covers a longer period and includes more eruptions than, for example, *Brühl et al.* [2015] or *Mills et al.* [2016]. The *Carn et al.* [2016] data set includes the mass of SO_2, height of SO_2 injection, Volcanic Explosivity Index (VEI) [*Newhall and Self*, 1982], vent altitude, and latitude and longitude of eruptions observed by satellites since 1979. Estimates of SO_2 loading into the atmosphere are based on satellite measurements in the ultraviolet (UV), infrared (IR), and microwave spectral bands. We only use explosive eruptions between 1980 and 2015, of VEI larger than 3 and for which the estimated SO_2 injection altitude is higher than 50% of the tropopause altitude. In addition, we use three basaltic eruptions: an eruptive event at Mount Etna (2011, Italy), and the large fissure eruptions of Laki (1783–1784) and Bárðarbunga (2014–2015) in Iceland. We estimate the mass eruption rate of all historical eruptions used on the basis of the observed height reached by their plumes using the integral volcanic plume model described in section 2.3. To do this, we specify atmospheric conditions retrieved from the National Centers for Environmental Prediction (NCEP)/National Center for Atmospheric Research (NCAR) reanalysis [*Kalnay et al.*, 1996], and all other parameters as in Table 1 except the vent altitude, and the gas content taken equal to 0.9 for the Bárðarbunga plume which contained little ash [*Schmidt et al.*, 2015].

Table 2 summarizes the date, location, mass, altitude, altitude range of injected SO_2, and the estimated mass eruption rate of 10 explosive eruptions from the *Carn et al.* [2016] data set as well as the three basaltic eruptions used. For the Laki (1783–1784) eruption, we use a mean plume altitude of 11 km corresponding to the range of plume altitudes of 9–13 km estimated by *Thordarson and Self* [2003] for explosive plumes during the first 3 months of the eruption, during which most of the SO_2 was released. Uncertainties in the altitude reached by volcanic SO_2 plumes are large, including when they are estimated using satellite measurements. For example, estimates from *Carn et al.* [2016] are often in the higher range of values found in *Brühl et al.* [2015] or *Mills et al.* [2016]. Another example is the Nabro (2011) eruption, for which *Bourassa et al.* [2013] report tropospheric plume altitudes of 13–16 km, while *Vernier et al.* [2013] and *Fromm et al.* [2013] report stratospheric altitudes of 16–19 km.

Last, in section 4, we use the *Sigl et al.* [2015] data set in addition to the *Carn et al.* [2016] data set to estimate SO_2 flux into the stratosphere. *Sigl et al.* [2015] use Greenland and Antarctic ice cores to reconstruct the mass of volcanic aerosols produced in the stratosphere by eruptions over the past 2500 years. Supporting information Figure S3 shows the distribution of erupted mass of SO_2 using these two data sets. The *Carn et al.* [2016] data set enables to characterize small stratospheric injections ($\leq$3 Mt (megatons) of SO_2), which occur with a frequency that is larger than the rate of decay of stratospheric sulfate aerosol and contribute strongly to the "stratospheric aerosol background" [*Solomon et al.*, 2011]. The *Sigl et al.* [2015] data set, on the other hand, enables to characterize large stratospheric injections ($\geq$3 Mt of SO_2) which occur with a frequency that is much smaller than the rate of decay of stratospheric sulfate aerosol and thus act as impulsive forcings.

Table 2. Subset of the Volcanic Eruptions Chosen to Test the Impact of Climate Change on Plume Height

Volcano	Date	Country	Latitude	Vent Altitude (km)	SO_2 Plume Altitude (km)	Estimated M_0 (kg s^{-1})	SO_2 (Mt)	$\Delta\tau$
El Chichón, A	29 Mar 1982	Mexico	17.4°N	1.2	17^{a}	1.310^{7}	0.75^{b}	9.210^{-2c}
El Chichón, B	4 Apr 1982	Mexico	17.4°N	1.2	28^{d}	3.010^{8}	7^{e}	9.210^{-2f}
Mt Pinatubo	15 Jun 1991	Philippines	15.0°N	1.7	$25^{g}(17–28)^{h}$	1.710^{8}	18^{i}	1.410^{-1j}
Manam	27 Jan 2005	Papua New Guinea	4.1°S	1.8	$24^{k}(18–24)^{l}$	$8.1\ 10^{7}$	0.14^{m}	$8.0\ 10^{-4n}$
Soufrière Hills	20 May 2006	Montserrat (UK)	16.7°N	0.2	$20^{o}(17–21)^{p}$	$4.1\ 10^{7}$	0.2^{a}	$2.2\ 10^{-3c}$
Kasatochi	7 Aug 2008	Russia	52.2°N	0.3	$15^{b}(10–18)^{d,e,i}$	$3.4\ 10^{7}$	2^{b}	1.510^{-3c}
Sarychev	16 Jun 2009	Russia	48.1°N	1.5	$17^{b}(11–17)^{d,e}$	$3.8\ 10^{7}$	1.2^{b}	2.610^{-3c}
Merapi	4 Nov 2010	Indonesia	7.5°S	3	$17^{b}(14–18)^{d,e}$	$5.5\ 10^{6}$	0.3^{b}	$1.0\ 10^{-3c}$
Nabro	13 Jun 2011	Eritrea	13.4°N	2.2	$18^{b}(10–19)^{d,e,j,k,l,m}$	$1.8\ 10^{7}$	0.68^{b}	$3.4\ 10^{-3c}$
Kelut	13 Feb 2014	Indonesia	8.0°S	1.7	$19^{b}(17–26)^{e}$	$2.9\ 10^{7}$	0.2^{b}	$2.5\ 10^{-3l}$
Laki	8 Jun 1783 to 7 Feb 1784	Iceland	64°N	1.7	$11\ (9–13)^{o}$	$3.7\ 10^{6}$	122^{o}	–
Etna	20 Aug 2011	Italy	37.7°N	3.4	9^{b}	$5.6\ 10^{5}$	0.004^{b}	–
Bárðarbunga	Sep 2014 to Dec 2014	Iceland	64.6°N	2	$5^{b}(3–5)^{p}$	$7.1\ 10^{4}$	4.3^{b}	–

[a] The top group consists of eruptions with relatively large stratospheric injections in the late 20th century. The middle group consists of eruptions with relatively small stratospheric injections in the early 21st century with a distinct footprint on climate [*Santer et al.*, 2015]. The bottom group consists of basaltic eruptions, either stratospheric or tropospheric. SO_2 mass and plume altitudes are taken from *Carn et al.* [2016], except for the Laki eruptions [*Thordarson and Self*, 2003], and the range indicated for plume altitude corresponds to estimated range from other studies, when available. We also indicate the stratospheric aerosol optical depth peak after the eruption, defined as the stratospheric aerosol optical depth of the month preceding the eruption subtracted from the first peak in the global monthly mean stratospheric aerosol optical depth in the 12 months following an eruption.

[b] *Carn et al.* [2016].

[c] *Sato et al.* [1993].

[d] *Brühl et al.* [2015].

[e] *Mills et al.* [2016].

[f] *Guo et al.* [2004].

[g] *Tupper et al.* [2007].

[h] *Prata et al.* [2007].

[i] *Waythomas et al.* [2010].

[j] *Fromm et al.* [2013].

[k] *Vernier et al.* [2013].

[l] *Bourassa et al.* [2013].

[m] *Clarisse et al.* [2014].

[n] *Rieger et al.* [2015].

[o] *Thordarson and Self* [2003].

[p] *Schmidt et al.* [2015].

2.2. Atmospheric Conditions

2.2.1. Choice of GCM, Period, and RCP Scenario

We retrieve the temperature (T), pressure (P), horizontal wind speed (V), and relative humidity (RH) profiles required for each run of the integral volcanic plume model. These fields are retrieved from an ensemble of three Coupled Model Intercomparison Project Phase 5 (CMIP5) GCMs:

1. BCC-CSM1.1 is the coarse resolution version of the Earth System Model (ESM, coupled climate-carbon cycle model) of the Beijing Climate Center Climate System Model (BCC-CSM) [*Wu et al.*, 2014]. The horizontal resolution is approximately 2.8125° × 2.8125° with 26 levels for the atmospheric component .
2. CanESM2 is the Earth system model of the Canadian Centre for Climate Modeling and Analysis [*Chylek et al.*, 2011]. The horizontal resolution is approximately 1.875° × 1.875° with 35 levels for the atmospheric component.
3. MPI-ESM-LR is the Earth system model of the Max Planck Institute (MPI) [*Giorgetta et al.*, 2013]. The horizontal resolution is approximately 1.875° × 1.875° with 47 levels for the atmospheric component.

We choose these GCMs because of the availability of long-term (2005–2300) climate projection outputs with a daily resolution (Table S1). Profiles of fields are drawn from GCM output over 8 to 15 pressure levels. Because the integral volcanic plume model uses height levels and is integrated with a vertical resolution of a few tens of meters, we also retrieve geopotential height (Z) profiles and interpolate the field profiles drawn from GCM results using a cubic interpolation scheme (after testing several interpolation methods). Because the duration of large explosive eruptions is typically of the order of 1 day [e.g., *Mastin et al.*, 2009], we use daily atmospheric variables, retrieved from 12 regions in which explosive eruptions potentially reaching the stratosphere [Volcanic Explosivity Index $\geqslant$3, *Newhall and Self*, 1982] most frequently occur (Figure 1 and Table S2). For each region we derive the spatially averaged daily atmospheric profiles. All GCM outputs are obtained from the Climate and Environmental Retrieval and Archive database (http://cera-www.dkrz.de/). We use [*Taylor et al.*, 2012] the following: (1) historical experiments where GCMs were run for the 1850–2005 period with imposed atmospheric composition (e.g., CO_2), solar forcing, aerosols, and land use changes inferred from observations and (2) Representative Concentration Pathways (RCP) experiments where GCMs were run with different forcing scenarios, in particular in terms of CO_2 concentrations but also in terms of other greenhouse gases, aerosols, and land use change. We use the RCP2.6, RCP4.5, and RCP8.5 experiments and the periods 2081–2100, 2181–2200, and 2281–2300.

We take our reference period to be 1981–2000, for which data are retrieved from the historical experiments. Our choice of RCP scenarios and periods allows us to explore the impact of a large range of greenhouse gas forcings [*Van Vuuren et al.*, 2011]:

1. For the RCP2.6 scenario, Earth radiative forcing peaks at +3 W m^{-2} (relative to preindustrial period) in the mid-21st century before decreasing (+2.6 W m^{-2} in 2100, $\simeq$+2 W m^{-2} in 2300). In the fifth assessment report (AR5), the International Panel on Climate Change (IPCC) project global mean surface air temperature anomalies in 2081–2100 relative to 1986–2005 were 1.0 ± 0.4, and 0.6 ± 0.3 in 2281–2300 (CMIP5 multimodel mean ± 1 standard deviation across individual models [*Collins et al.*, 2013]).
2. For the RCP4.5 scenario, the radiative forcing peaks at +4.5 W m^{-2} in 2100 and is stable in the following centuries. Projected temperature anomalies for this scenario are 1.8 ± 0.5 in 2081–2100 and 2.5 ± 0.6 in 2281–2300.
3. For the RCP8.5 scenario, the radiative forcing peaks at +8.5 W m^{-2} in 2100, is +12 W m^{-2} in the mid-23rd century, and is steady afterward. Projected temperature anomalies for this scenario are 3.7 ± 0.7 in 2081–2100 and 7.8 ± 2.9 in 2281–2300.

Current CO_2 emissions slightly exceeded the RCP8.5 scenario over 2010–2014 [*Sanford et al.*, 2014]). For each period and RCP experiment, we use only one run for the GCMs with multiple runs available. We make this choice because for the 22nd and 23rd centuries, most GCMs only have outputs for the last 20 years of these centuries from a single run available (Table S1). For consistency, we used the same period duration and number of runs for the 20th and 21st centuries.

2.2.2. Performance of Chosen GCMs

There is large variability in the capabilities of GCMs for reproducing past climate, as well as in their predictions of future climate. The performance of given GCMs also strongly depend on region, field variable (e.g., temperature), and altitude range [*Gleckler et al.*, 2008; *Flato et al.*, 2013]. The three GCMs (BCC-CSM1.1, CanESM2, and MPI-ESM-LR) we select for this study must perform well for all four fields (T, V, RH, and Z) and in each of the 12 regions chosen. Following *Gleckler et al.* [2008] , we compare how GCM historical runs reproduce climate over the 1960–2000 period, our reference period for GCM ranking. In addition to our selected three GCMs we use 13 other GCM for this evaluation analysis since we are interested in the relative performance of the selected GCMs within a model ensemble. The 16 GCMs (Table S1) are selected following previous GCM evaluation studies [e.g., *Flato et al.*, 2013]. We choose the NCEP-NCAR reanalysis [*Kalnay et al.*, 1996] as a reference data set but obtain very similar results using the ERA40 reanalysis [*Uppala et al.*, 2005]. This section provides a brief overview of our evaluation procedure and main results. The reader is referred to the supporting information (Text S1) for further details.

GCMs are compared to the reference data set on the basis of their root-mean-square errors (RMSE) assessed on (i) the monthly average of a field (T, V, RH or Z), (ii) the monthly standard deviations, over time, in a field, and (iii) the frequency of occurrence of one field characteristic profiles. For the latter metric, for a given region, month, and field, we demean and normalize daily profiles by substracting the monthly mean and dividing by the monthly standard deviation, at each altitude. We then identify characteristic profiles and their frequency of occurrence in the reference data set using a Self-Organizing Map algorithm (SOM) [*Kohonen*, 1982]. Next, for each demeaned and standardized profile of a GCM, we find the best matching profile among the characteristic profiles of the reference data set. We can then compare the frequency of occurrence of a characteristic profile in a GCM and in the reference data set [*Radić et al.*, 2015]. More details on this metric are given in the supporting information. Since we are interested in the relative model performance, we define the relative RMSE as the

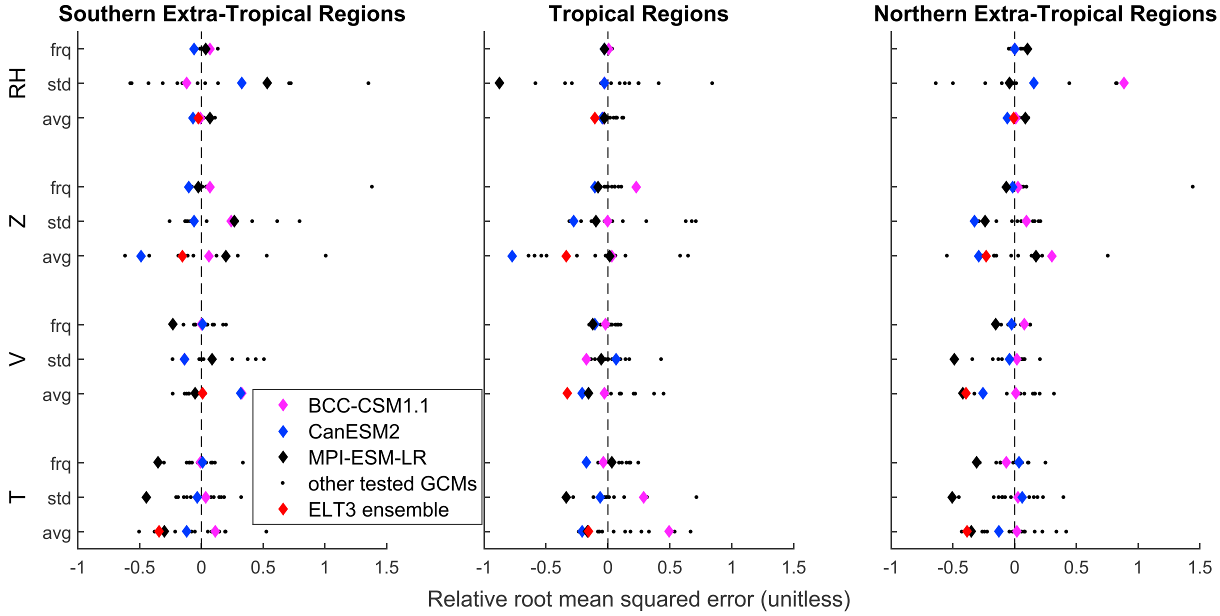

Figure 3. Relative root mean square error (unitless, relative to the GCM median error) for the *T*, *V*, *Z*, and RH fields, the three evaluation metrics (average, standard deviation, and frequency of characteristic patterns noted "avg," "std," and "frq", respectively, on the figure) and the three groups of regions. Small black dots show the relative error for the 16 GCMs tested (Table S1). Diamond symbols show the three GCMs selected to be used in this study (BCC-CSM1.1, CanESM2, and MPI-ESM-LR) and their ensemble (ELT3). A negative error (left of the dashed line) indicates that a GCM performs better than the median GCM. More details on the GCM evaluation procedure are given in supporting information Text S1.

error relative to the median error of the 16 GCMs. In this way, a relative model error of, for example, 0.5 means that the GCM has a 50% larger error than the median model error. Figure 3 shows the relative RMSE for the three GCMs used for this study and their ensemble across all evaluation metrics. For simplicity, we grouped the 12 regions into three groups of regions: northern extratropical, tropical, and southern extratropical region.

For all metrics, two of our selected GCMs (MPI-ESM-LR and Can-ESM2) perform better than the median model, especially for the tropical and northern high-latitude regions. MPI-ESM-LR outperforms most GCMs for temperature related metrics. For BCC-CSM1.1, errors are generally close to or larger than the GCM median error. The error of the ensemble of the chosen three GCMs (ELT3) is always below the GCM median error, for errors on average fields. In particular, ELT3 outperforms most GCMs in reproducing the mean temperature and horizontal wind speed profile (except for wind over the southern extratropical regions). ELT3 is sometimes outperformed by CanESM2 or MPI-ESM-LR. However, using this ensemble for our study will allow us to better account for uncertainties related to spread in GCMs projections of future climate. Sensitivity of our results to the choice of GCMs will be further discussed in section 4.

2.3. Integral Volcanic Plume Model

To compute the height reached by a volcanic plume, we use an integral volcanic plume model described in *Degruyter and Bonadonna* [2012], which is based on the 1-D buoyant plume model of *Morton et al.* [1956] adapted by *Woods* [1988] for explosive eruptions. The model also includes the effects of atmospheric wind and humidity on the plume rise [*Bursik*, 2001; *Glaze et al.*, 1997]. We use the maximum height reached by the plume H (also called overshoot height, Figure 4), but we verified that using the height of the neutral buoyancy level H_b instead does not impact our results. Plume properties (e.g., temperature, velocity, or relative humidity) profiles across the plume are assumed to be top hat in shape and thus depend only on the position along the plume centerline s (Figure 4). Plume rise is governed by conservation equations for mass, momentum, and energy rates [*Degruyter and Bonadonna*, 2012].

Turbulent motions mix surrounding atmosphere into a rising plume. To characterize this critical phenomenon, we employ the entrainment hypothesis [*Morton et al.*, 1956], modified to account for wind effect [*Hewett et al.*, 1971], to specify the inflow entrainment velocity normal to the centerline u_ϵ as follows:

$$u_\epsilon = \alpha|u - V\,sin(\phi)| + \beta|V\,cos(\phi)|\,. \tag{4}$$

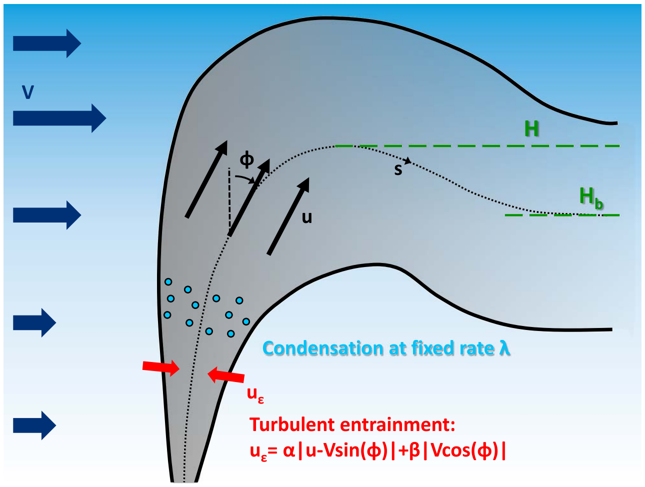

Figure 4. Cartoon of a volcanic plume rising in the atmosphere and problem definition for the integral volcanic plume model developed in section 2.3. Plume properties, such as the plume velocity u, depend only on the distance along the plume centerline s, and plume property profiles are top hat (constant inside the plume and null outside). The inflow of atmospheric air into the plume u_ϵ is proportional to the radial gradient of axial velocity between the plume and the atmosphere ($|u - V\sin(\phi)|$) and to the radial gradient of orthoaxial velocity ($|V\cos(\phi)|$) where ϕ, the local plume deflection with respect to the vertical, defines the local axial direction. The green dashed lines show the maximum plume altitude H and the altitude of neutral buoyancy H_b.

Here u is the average axial velocity of the plume, and ϕ is the plume deflection with respect to the vertical direction (Figure 4). The parameter α is the radial entrainment coefficient [*Morton et al.*, 1956] and relates u_ϵ to the radial gradient of axial velocity. The parameter β is the wind entrainment coefficient [*Hewett et al.*, 1971] and relates u_ϵ to the radial gradient of normal velocity. The major effect of wind is to enhance entrainment rates. On the basis of the experiments of *Carazzo et al.* [2014], we take $\alpha = 0.1$ and $\beta = 0.7$ unless otherwise specified. These values are within the range commonly used in buoyant plume models [e.g., *Costa et al.*, 2016]. Integral volcanic plume models capture the first-order effects of atmospheric temperature and wind stresses variations on the rise of the plume [e.g., *Degruyter and Bonadonna*, 2012; *Woodhouse et al.*, 2013; *Mastin*, 2014; *Folch et al.*, 2016]. Uncertainties on the entrainment coefficients (Table 1) are the main sources of uncertainty on the plume height [e.g., *Mastin*, 2014; *Woodhouse et al.*, 2015; *Bonadonna et al.*, 2015; *Costa et al.*, 2016] and will be discussed in section 4.

In addition to temperature and wind, atmospheric humidity can impact the plume rise. Entrained water vapor can condense inside a plume, leading to an additional buoyancy flux related to release of latent heat [*Morton*, 1957; *Woods*, 1993]. To include these effects, we follow *Glaze et al.* [1997] and assume that water vapor condensation inside the plume occurs at a specified constant rate λ when water vapor pressure is above the saturation pressure. The reader is referred to *Degruyter and Bonadonna* [2012] for further details on the integral volcanic plume model. How to most accurately capture the effects of humidity on plume rise in integral models is a challenge that is largely unexplored. Furthermore, simulation of humidity and cloud formation is one of the main challenges for GCMs [*Flato et al.*, 2013]. Consequently, in this study, the impact of projected changes in relative humidity will be discussed in section 4 but is not considered (i.e., $\lambda = 0$) in our main results (section 3).

For given eruption source conditions, region, period, and RCP scenario, the volcanic plume maximum height depends on the exact weather conditions during the eruption. As future mean weather conditions are projected with a large range of uncertainty, we apply a method that allows us to assess the probability of occurrence of most prevailing (characteristic) weather conditions in terms of temperature, wind speed, relative humidity, and geopotential height. To this end, we use a SOM algorithm to cluster the GCMs daily profiles from each 20 year period into $\simeq$60 representative profiles, each of those having an associated frequency of occurrence over 20 years. We then run the integral volcanic plume model for each representative profile to obtain a probability distribution of the plume altitude using the frequency of occurrence of each profile (Figure 2b). This distribution accounts for both variability in atmospheric conditions as simulated by one GCM within a 20 year period (e.g., due to seasonal cycle) and the inter-GCM variability as we use a three-model ensemble.

In addition to plume height, for each characteristic profile identified by the SOM algorithm, we estimate the tropopause height by interpolating the temperature profile and finding the lowest altitude at which the temperature lapse rate is less than 2 K km^{-1}, for at least 2 km (following the World Meteorological Organization definition). Although the vertical resolution of GCM data sets used is coarser than the multidecadal changes in tropopause height, previous studies demonstrate that estimates on the basis of interpolation of coarse temperature profiles are reliable to assess multidecadal changes in tropopause height [e.g., *Santer et al.*, 2003].

3. Results

To understand how global warming might impact the height reached by volcanic plumes, we first analyze distinct effects of projected changes in temperature and geopotential height profiles (which control the lapse rate) and horizontal wind speed profiles for two regions (one high latitude, Chile, and one tropical, Philippines) under strong greenhouse gas forcing (scenario RCP8.5). We then assess the combined impacts of changes in temperature, geopotential height, and wind for the same forcing and regions and summarize results for all regions (Figure 1), periods (1981–2000, 2081–2100, 2181–2200, and 2281–2300), and forcing scenarios (RCP2.6, RCP4.5, and RCP8.5). Finally, we illustrate our results by projecting changes in the height of historical eruptions if they were to occur under future climate conditions.

3.1. Impact of Temperature and Geopotential Height Changes Under RCP8.5

In this section, we fix the horizontal wind speed to the average of the reference period (1981–2000) for each region. Figure 5 shows the temperature as a function of geopotential height in Chile (a) and in the Philippines (b), for the reference (1981–2000), 2081–2100, and 2281–2300 periods. For both regions, the temperature increases with time in the troposphere and decreases in the stratosphere, and the tropopause height increases. In the tropical region (Philippines), changes in median temperature and tropopause height from one period to another are large compared to the seasonal and interannual variability over each period. In contrast, the changes are smaller compared to variability in the high-latitude region (Chile), mostly because of the higher seasonality. Between the late 23rd century and the reference period, the tropospheric lapse rate is projected to decrease by $0.9\ \mathrm{K\ km^{-1}}$ in the Philippines and by $0.4\ \mathrm{K\ km^{-1}}$ in Chile. The stratospheric lapse rate is projected to increase by $\simeq 1\ \mathrm{K\ km^{-1}}$ on average between the tropopause and $\simeq$30 km altitude, which results in a slightly positive lapse rate in the lower stratosphere in Chile, for the 2281–2300 period (where the lapse rate is defined as $\Gamma = -\frac{dT}{dz}$).

Volcanic plume heights vary with projected temperature and geopotential height changes (Figures 5c and 5d). In particular, where the lapse rate decreases, plume height decreases and vice versa. In the Philippines, for mass eruption rates of order of magnitude $10^7\ \mathrm{kg\ s^{-1}}$, plume heights are projected to decrease by 2–3 km in the upper troposphere. Decrease in tropospheric plume height is weaker (<1 km) and less significant in Chile. For both regions, stratospheric plume ($M_0 \gg t10^7\ \mathrm{kg\ s^{-1}}$) heights are predicted to increase by $\simeq$2 km, with a more significant increase in the tropical region. The uncertainty in plume height due to temperature variability over one period is small ($\simeq$1–2 km for both regions).

The ratio of the maximum plume altitude to the tropopause altitude (H^*) declines for both regions and all M_0, as greenhouse gas forcing increases (Figures 5e and 5f). In the Philippines, for an eruption whose median H^* was equal to 1 in the reference period, H^* decreases by 0.2–0.3 in 2281–2300. Similar changes are predicted for Chilean plumes but are smaller and less significant due to relatively small decreases in tropospheric plume height and larger temperature variability. In the stratosphere, although plume heights increase, H^* decreases by $\simeq$0.2–0.3 for both regions because the tropopause height increases over the same period.

3.2. Impact of Horizontal Wind Speed Changes Under RCP8.5

We now fix the temperature and geopotential height to their average values for the reference period for each region while we apply daily wind profiles from GCM runs in the plume model. Overall, we observe no significant change in projected wind profiles in either region (Figures 6a and 6b). For example, in Chile, there is a decrease in median tropospheric wind speed and an increase in median stratospheric wind speed. However, these changes are small relative to the wind variability over one period. Similar conclusions apply to the Philippines, where the winds are weaker and changes are smaller relative to Chile. For both regions, the wind speed variability in time increases with greenhouse gas forcing.

Variations of H^* (Figures 6c and 6d) only reflect variations in plume height since the temperature profiles, and thus the tropopause height, are constant. For a given M_0 and over one period, wind variability causes H^* to vary by 0.1 to 0.4 around its median, which makes the changes in H^* driven by long-term wind speed changes in response to increasing greenhouse forcing negligible compared to these uncertainties.

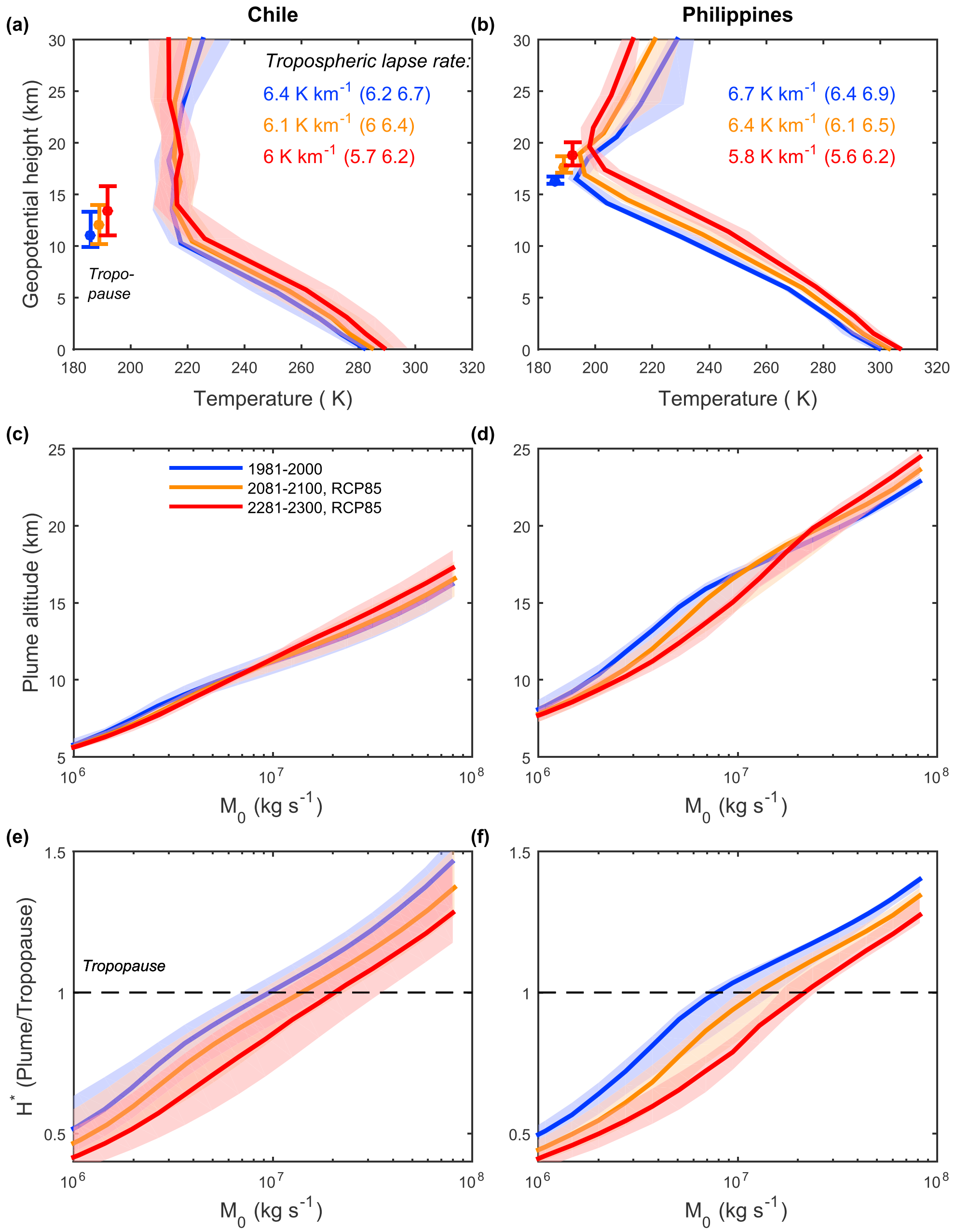

Figure 5. Impacts of projected changes in temperature and geopotential height on volcanic plume height for RCP8.5 (wind fixed to reference period average): Left and right columns show results for the Chile and Philippine regions, respectively. (a, b) The temperature as a function of the geopotential height. Bold lines show the median temperature, and shaded areas show the interval between the 5th and 95th quantiles. The median tropopause height is shown by a square on the top row, with an error bar showing the interval between the 5th and 95th quantiles. Blue, orange, and red correspond to the reference period (1981–2100), 2081–2100 RCP8.5, and 2281–2300 RCP8.5 projections, respectively. The values of the median tropospheric lapse rate are indicated in Figures 5a and 5b with 5th and 95th quantiles indicated in parentheses. (c, d) The maximum plume altitude (*H*) as a function of the mass eruption rate. (e, f) H^*, the ratio of the maximum plume height to tropopause height, as a function of the mass eruption rate.

3.3. Impact of Combined Changes of Temperature, Geopotential Height, and Horizontal Wind Speed Under RCP8.5

We now analyze the effect of combined changes in temperature, geopotential height, and wind speed. To facilitate the discussion, we define a normalized mass eruption rate $M_0^* = \frac{M_0}{M_0^{\text{tp,ref}}}$, where $M_0^{\text{tp,ref}}$ is the median

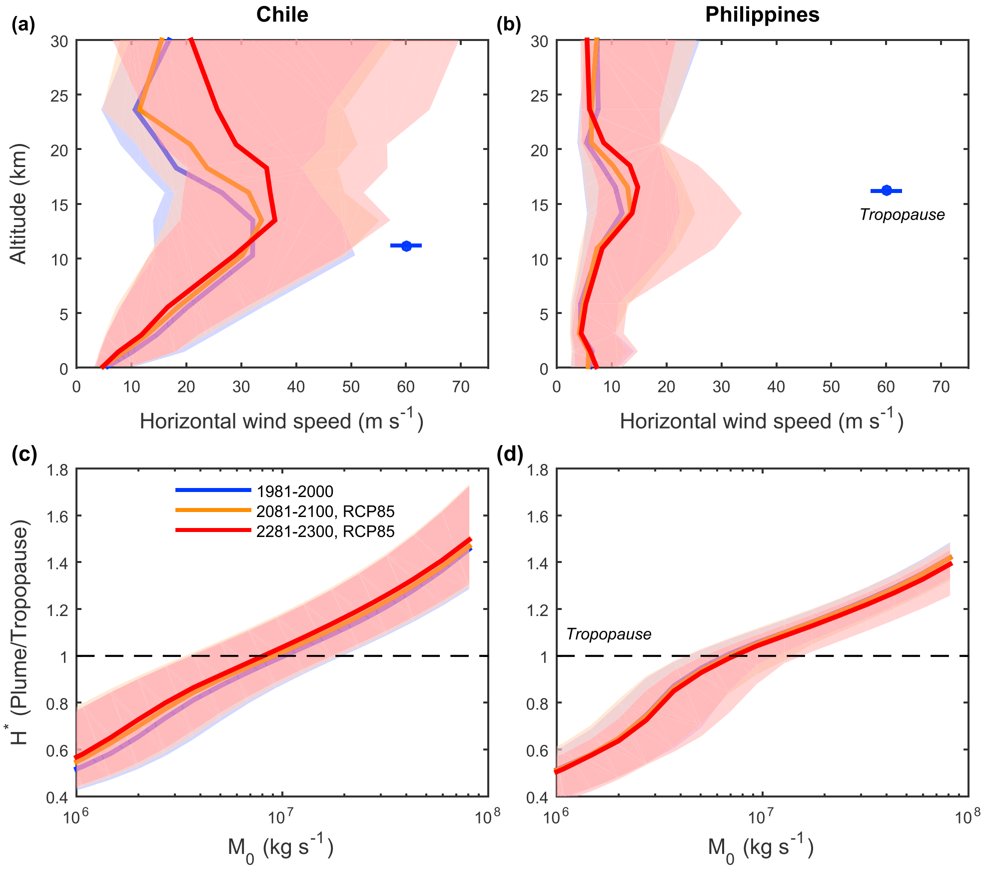

Figure 6. Impact of projected changes in wind speed on volcanic plume height for RCP8.5 (temperature and geopotential height fixed to reference period average): The temperature and geopotential height profiles are fixed to their averages for the reference period. (a, b) The horizontal wind speed as a function of the geopotential height. (c, d) H^* as a function of the mass eruption rate, with a fixed tropopause altitude. Regions, color, and shading are the same as for Figure 5.

critical mass eruption rate for which $H^* = 1$ for the reference period (1981–2000). Thus, our normalization for M_0 is dependent on the region but indicates variations in M_0 required to reach the tropopause.

Figure 7 shows H^* as a function of M_0^*. Evolution of H^* as the greenhouse gas forcing increases is the same as when varying the temperature and geopotential height only (Figure 5). For a given M_0^* and period, uncertainties on H^* originating from variability of temperature, geopotential height, and wind speed are comparable to those obtained when varying the wind speed only (Figure 6). For example, in the Philippines, the median H^* decreases by up to $\simeq$0.15 in the upper troposphere, for the late 21st century, and up to $\simeq$0.25 for the 23rd century (RCP8.5). Decrease of plume height and increase of tropopause height contribute equally to changes in H^* and result in the increase of the critical mass eruption rate required to cross the tropopause. It is increased by a factor of 1.65 for the late 21st century compared to the reference period and a factor of 2.8 for the 23rd century. We observe similar trends for Chile (Figure 7a), although the magnitude of changes in H^* or critical M_0^* to reach the tropopause are smaller.

3.4. Summary: Results for All Investigated Regions, Periods, and Scenarios

We summarize our results with two key values. The first is the median value of H^* for which $M_0^* = 1$ (horizontal dotted lines in Figure 7, and Table 3). The second is the median value of M_0^* for which $H^* = 1$ (vertical dashed lines in Figure 7, and Table 4). For the reference period, we estimate the 99% confidence interval on the median H^* for which $M_0^* = 1$ or median M_0^* for which $H^* = 1$ by using a bootstrap method (cf. supporting information Text S2).

For $M_0^* = 1$, H^* mostly decreases by 0 to 0.25 relative to the 1981–2000 reference period (Table 3). For the RCP2.6 scenario, H^* increases by 0 to 0.03 in some extratropical regions and always decreases for tropical

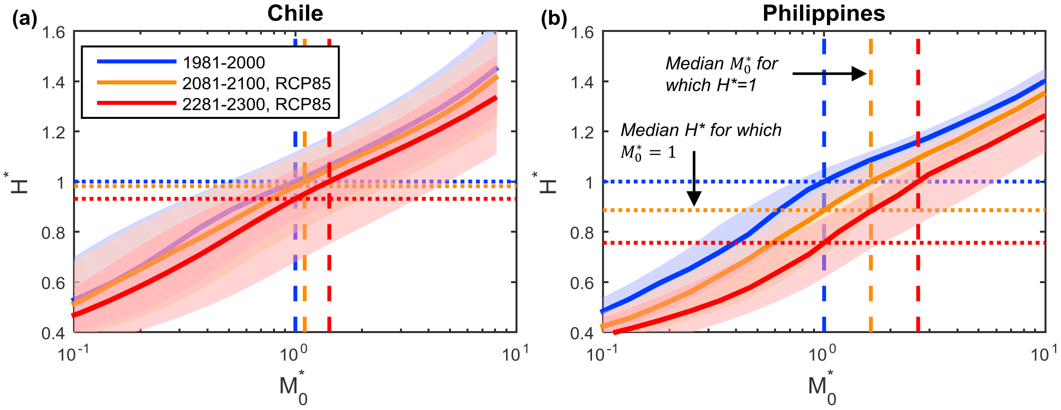

Figure 7. Changes in H^* as a function of the dimensionless mass eruption rate M_0^* (normalized to the median mass eruption rate required to reach the tropopause in 1981–2000) for RCP8.5: Result for (a) Chile and (b) Philippines. Bold lines show the median, and shadings show the interval between the 5th and 95th quantiles. Blue, orange, and red correspond to the reference period (1981–2100), 2081–2100 RCP8.5, and 2281–2300 RCP8.5 projections, respectively. Dotted lines of corresponding colors show the median value of H^* reached in $M_0^* = 1$ (i.e., the median mass eruption rate for which the tropopause is reached in 1981–2000). Dashed lines of corresponding colors show the median value of M_0^* required to reach $H^* = 1$ (i.e., the tropopause).

regions. Decreases in H^* are stronger and more statistically significant for tropical regions, higher RCP scenarios, and more distant future for RCP4.5 and RCP8.5, for which the radiative forcing does not stabilize before 2300 (cf. section 2.2 and *Van Vuuren et al.* [2011]). For RCP8.5, the median H^* reached with $M_0^* = 1$ decreases by $\simeq$0.2 in tropical regions and $\simeq$0.1 in extratropical regions, compared to the reference period. Changes are statistically significant for all tropical regions and most extratropical regions for RCP8.5 and for tropical regions for RCP4.5.

Table 4 shows the median M_0^* for which $H^* = 1$. The median critical mass eruption rate required to reach the tropopause generally increases by a factor of up to 2.8 depending on the region, period, and scenario. As for Table 3, changes are more significant for tropical regions, stronger radiative forcing, and time periods further away in the future. In particular, for the RCP8.5 scenario, the critical mass eruption rate is increased by a factor of 2 to 2.8 in tropical regions for the 22nd and 23rd centuries and 1.25 to 2 in extratropical regions. Again, for this scenario, changes are statistically significant in all tropical regions and most extratropical regions.

Table 3. H^* Reached for $M_0^* = 1$, i.e., the Median Plume Altitude, Relative to the Tropopause Height, Reached for a Mass Eruption Rate Equal to the One Required to Reach the Tropopause in 1981–2000[a]

	2081–2100			2181–2200			2281–2300		
	RCP2.6	RCP4.5	RCP8.5	RCP2.6	RCP4.5	RCP8.5	RCP2.6	RCP4.5	RCP8.5
Chile	1	0.99	0.98	1	1	**0.92**	0.99	0.99	**0.93**
New Zealand	0.99	0.98	0.97	0.99	0.97	**0.92**	1.01	0.97	**0.88**
Ecuador	**0.96**	**0.94**	**0.89**	0.97	**0.94**	**0.82**	**0.97**	**0.93**	**0.78**
Indonesia	0.98	**0.96**	**0.92**	0.99	**0.96**	**0.83**	0.99	**0.95**	**0.8**
Philippines	**0.95**	**0.96**	**0.89**	**0.94**	**0.93**	**0.79**	**0.96**	**0.94**	**0.75**
Central America	**0.96**	**0.94**	**0.89**	**0.96**	**0.92**	**0.82**	**0.96**	**0.94**	**0.79**
African Ridge	**0.97**	**0.96**	**0.91**	**0.98**	**0.95**	**0.83**	0.99	**0.93**	**0.8**
Japan	0.99	**0.98**	**0.96**	0.99	**0.96**	**0.94**	1	**0.98**	**0.92**
Cascade	1	0.99	**0.96**	0.99	**0.98**	**0.93**	1.02	**0.99**	**0.92**
Kamchatka	1.01	0.99	0.94	1.01	1	**0.87**	1.02	0.98	**0.88**
Aleutians	1	1	**0.96**	1.03	1.03	**0.9**	1.01	1	**0.87**
Iceland	1	0.99	**0.94**	0.99	0.99	**0.9**	1	0.98	**0.88**

[a] The table provides the values for each region (rows) and period and scenario (columns) considered in this study. Bold values indicate 99% significant changes relative to the reference period (cf. supporting information Text S2 for details on the significance test).

Table 4. Same as Table 3 But Showing the Median M_0^* Required to Reach $H^* = 1$

	2081–2100			2181–2200			2281–2300		
	RCP2.6	RCP4.5	RCP8.5	RCP2.6	RCP4.5	RCP8.5	RCP2.6	RCP4.5	RCP8.5
Chile	0.98	1.04	1.1	0.99	1.01	**1.53**	1.05	1.08	**1.42**
New Zealand	1.09	1.15	1.18	1.03	1.19	**1.57**	0.95	1.19	**1.85**
Ecuador	**1.24**	**1.32**	**1.66**	**1.14**	**1.33**	**2.13**	**1.17**	**1.37**	**2.46**
Indonesia	**1.12**	**1.23**	**1.5**	1.09	**1.24**	**2.11**	1.06	**1.29**	**2.52**
Philippines	**1.32**	**1.25**	**1.65**	**1.34**	**1.39**	**2.29**	**1.21**	**1.3**	**2.8**
Central America	**1.24**	**1.38**	**1.79**	**1.25**	**1.52**	**2.41**	**1.21**	**1.37**	**2.75**
African Ridge	**1.14**	**1.21**	**1.59**	**1.11**	**1.27**	**2.27**	**1.08**	**1.41**	**2.44**
Japan	1.04	1.1	**1.23**	1.04	**1.2**	**1.25**	0.98	**1.11**	**1.42**
Cascade	0.99	1.05	**1.29**	1.04	**1.1**	**1.44**	0.9	**1.08**	**1.53**
Kamchatka	0.95	1.06	1.36	0.93	0.99	**1.86**	0.88	1.09	**1.92**
Aleutians	1.01	1	**1.2**	0.86	0.87	**1.69**	0.97	1.02	**1.84**
Iceland	0.99	1.05	**1.37**	1.04	1.04	**1.67**	0.99	1.11	**1.94**

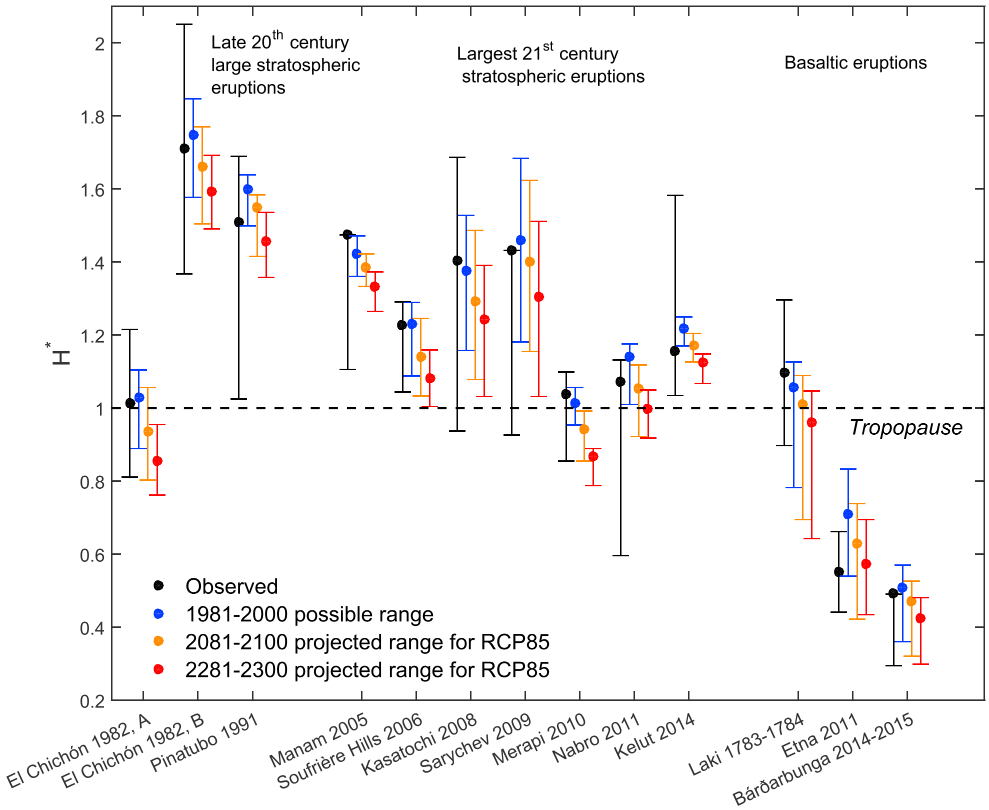

Figure 8. Observed and projected H^* for past volcanic eruptions (Table 2): Parameters for eruptions shown are listed in Table 2. The observed H^*, taken from *Carn et al.* [2016], is shown in black, with vertical bars showing the estimated uncertainty based on height estimates from different studies. We assume a relative uncertainty in plume height of ±20% where we could not find estimates different from *Carn et al.* [2016]. Blue, orange, and red dots show the predicted median H^* for the 1980–2000, 2081–2100 (RCP8.5), and 2281–2300 (RCP8.5) periods, with vertical bars showing the 5th and 95th quantiles. The horizontal dashed line indicates the tropopause, which corresponds to $H^* = 1$.

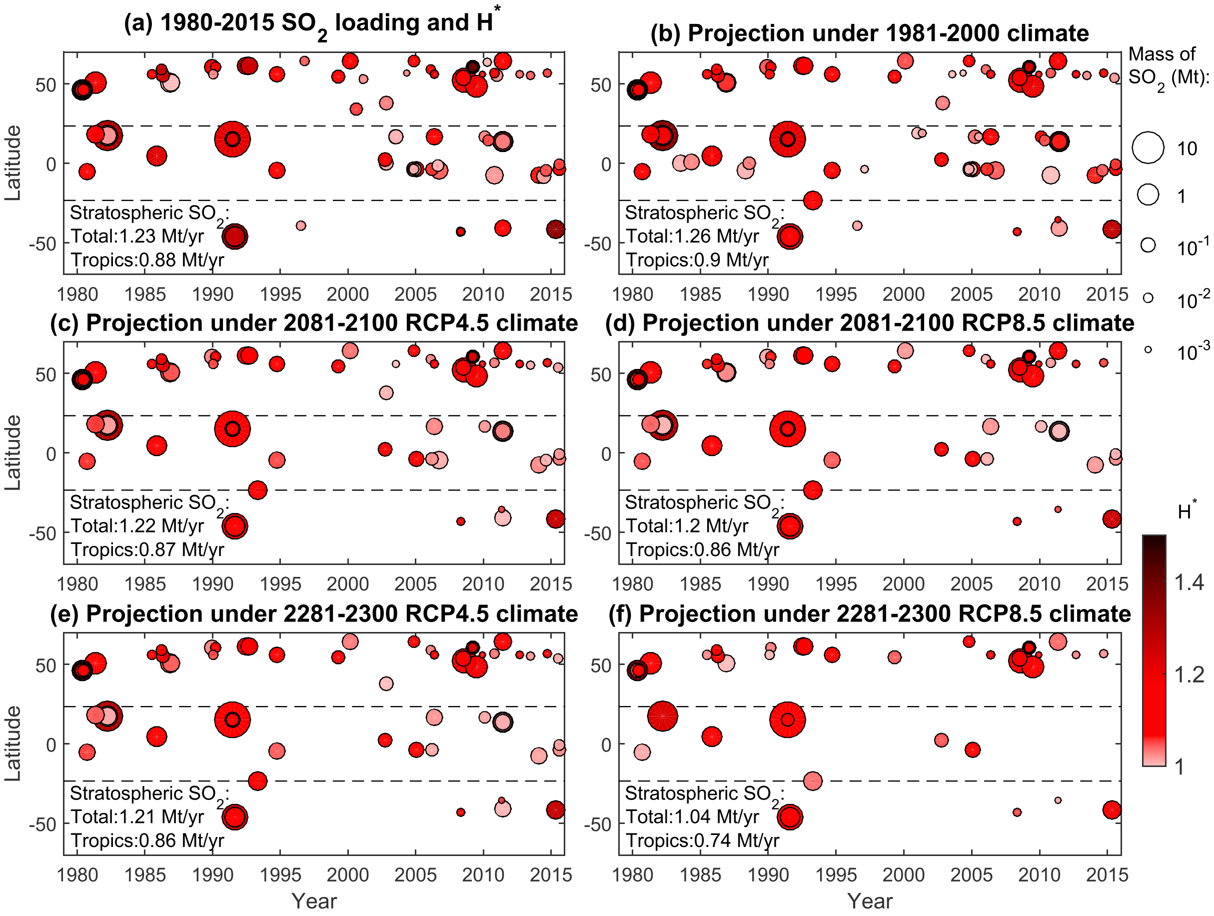

Figure 9. Same as Figure 8 but showing observed and projected H^* (color scale) as a function of time and latitude for all eruptions retained in the *Carn et al.* [2016] data set (dashed lines show the tropics). The size of the circles is proportional to the logarithm of the mass of SO_2 injected. Only stratospheric injections ($H^* \geqslant 1$) are shown. (a) The original *Carn et al.* [2016] data set. (b–f) We assume that the same sequence of eruptions occur (i.e., same source parameters) but use climate conditions representative of the labeled period and RCP scenario. For Figures 9b–9f, we used the median H^* for each eruption. The total and tropical volcanic flux of SO_2 into the stratosphere are indicated on each panel.

Values in Tables 3 and 4 are unchanged if we use the plume neutral buoyancy height H_b instead of the maximum plume height H (Figure 4) to define H^*.

3.5. Height Projections for Past Eruptions

To illustrate the effects of changes in volcanic plume and tropopause height, we first test how the height of 13 historical eruptions (Table 2) would change relative to the tropopause height as a consequence of greenhouse gas emissions. For each eruption, Figure 8 shows H^* inferred from *Carn et al.* [2016] and predicted values for the 1981–2000 reference period, 2081–2100 (RCP8.5), and 2281–2300 (RCP8.5). Atmospheric conditions used to predict H^* are associated with the region closest to the volcano considered except for the Etna eruption for which we retrieved reanalysis and GCM atmospheric profiles over Sicily (Figure 1 and Table S2). Eruptions with H^* above 1 cross the tropopause. The observed H^* generally lies within the range predicted using GCM historical runs for the 1981–2000 period. Predicted H^* for the late 21st century for the RCP8.5 scenario is lower than that which is predicted for the reference period. For two eruptions (El Chichón 1982 A and Merapi 2010), the predicted median H^* is below 1, indicating that the probability that the eruption will cross the tropopause is less than 50%. For the late 23rd century and a RCP8.5 scenario, the median H^* for four eruptions is below 1, with a probability to cross the tropopause of less than 5% for El Chichón 1982 A and Merapi 2010. The El Chichón 1982 B and Pinatubo eruptions remain largely above the tropopause, although H^* decreases for these eruptions as well. The value of H^* for analyzed basaltic eruptions also decreases. In particular, our results suggest that a Laki-type eruption would have less than 50% chance of crossing the tropopause in between 2100 and 2300, under the RCP8.5 scenario.

Figure 8 illustrates the impact of global warming on different size and type of plumes but does not reflect that smaller eruptive plumes (e.g., Merapi 2010) are more frequent than larger eruptive plumes (e.g., Pinatubo 1991). Accordingly, we project H^* for the subset of eruptions from the *Carn et al.* [2016] data set described in section 2.1 (i.e., in particular, VEI $\geqslant$ 3 and observed $H^* \geqslant 0.5$). Figure 9a shows the observed H^* and mass of injected SO_2 as a function of latitude and time. Figures 9b–9f show median H^* prediction under a 1981–2000, 2081–2100, and 2281–2300 climate (RCP4.5 and RCP8.5 for future periods). We show only stratospheric plumes (i.e., for which $H^* \geqslant 1$) and indicate on each panel the corresponding estimate for the global and tropical volcanic fluxes of SO_2 into the stratosphere. There is again a good agreement between H^* calculated from the *Carn et al.* [2016] data set (Figure 9a) and the values calculated for the reference period climate, using GCM historical runs (Figure 9b). For the reference period, the total flux of volcanic SO_2 into the stratosphere is 1.26 Mt/yr, about 0.9 Mt/yr of which are injected in the tropics. Under a 2081–2100 climate evolving under a RCP4.5 or RCP8.5 scenario, or 2281–2300 climate under RCP4.5, we find that there would be $\simeq$15–20 fewer eruptions reaching the stratosphere, on average, with most of the eruptions shifted below the tropopause being in the tropics. However, the flux of volcanic SO_2 into the stratosphere would only decrease by 0.04–0.06 Mt/yr (or 3 to 5%) for the total flux and 0.03–0.04 Mt/yr (or 3 to 4%) for the tropics. For a 2281–2300 climate under a RCP8.5 scenario, $\simeq$40 eruptions out of $\simeq$200 in this data set would be tropospheric rather than stratospheric. The corresponding reduction in the SO_2 injected into the stratosphere is 0.22 Mt of SO_2/yr (17%), 0.16 Mt of SO_2/yr (18%) of which would occur in the tropics. Last, for eruptions that remain in the stratosphere, H^* decreases by 0.1–0.4 depending on the time period and scenario considered.

4. Discussion

4.1. Mechanisms Driving Changes in Plume and Tropopause Heights

Under a RCP4.5 or RCP8.5 scenario, GCM projections imply that eruptions must have a larger mass eruption rate to reach the tropopause. This result is a consequence of (i) a decrease in tropospheric volcanic plume height and (ii) an increase in the tropopause height. The decrease in tropospheric plume height is a consequence of the decrease in tropospheric temperature lapse rate (Figure 5). Indeed, there is a remarkable agreement between the decrease in plume height predicted by applying change in tropospheric temperature lapse rate in equations (1) and (2) and decrease in plume height predicted by our volcanic plume model using daily profiles of temperature, wind speed, and relative humidity. When fixing temperature profiles but varying horizontal wind speed (Figure 6), we observe no large change in the median plume height but an increased difference between the 5th and 95th quantiles of plume height probability distribution. Horizontal wind speed is thus a source of uncertainty on plume height for a particular eruption, but multidecadal changes in wind speed in response to greenhouse gas emissions do not drive any significant shift of the plume height probability distribution. Our results apply to both explosive silicic eruption plumes and thermal plumes related to basaltic eruptions (Figure 8).

Although our results rely on GCM predictions, they require only a decrease of tropospheric lapse rate and an increase of the tropopause height. Both CMIP5 GCMs and observations exhibit a decrease of the tropospheric temperature lapse rate in the tropics, over the 1960–2010 period [*Fu et al.*, 2011; *Simmons et al.*, 2014; *Sherwood and Nishant*, 2015]. In particular, CMIP5 GCMs simulate well the shape of warming rate profiles in the tropical troposphere, which controls the change in lapse rate [*Mitchell et al.*, 2013]. Also, an increase of the tropopause height is found consistently in GCMs and observations [e.g., *Santer et al.*, 2003].

A key question is to assess how past changes in temperature lapse rate and tropopause height have impacted the rise of volcanic plumes. *Glaze et al.* [2015] discuss how the height of a plume produced by a flood basalt eruption would change in an atmosphere typical of the Miocene. They suggest that a warmer atmosphere would cause a decrease in plume height. The near-vent atmospheric temperature controls the temperature difference between the erupted ash-gas mixture and the atmosphere, and thus the plume source buoyancy flux. However, near the vent, the plume is hundreds of degrees kelvin warmer than the atmosphere and the source buoyancy flux would thus not be significantly affected by a few degrees kelvin change of the atmospheric temperature. In addition, the plume height only weakly depends on the plume source buoyancy flux relative to the atmospheric stratification (equation (1)). A change in the mean tropospheric temperature without a change in the lapse rate would also affect the stratification (equation (2)), but again it would be negligible as atmospheric temperature is of the order of hundreds of degrees kelvin.

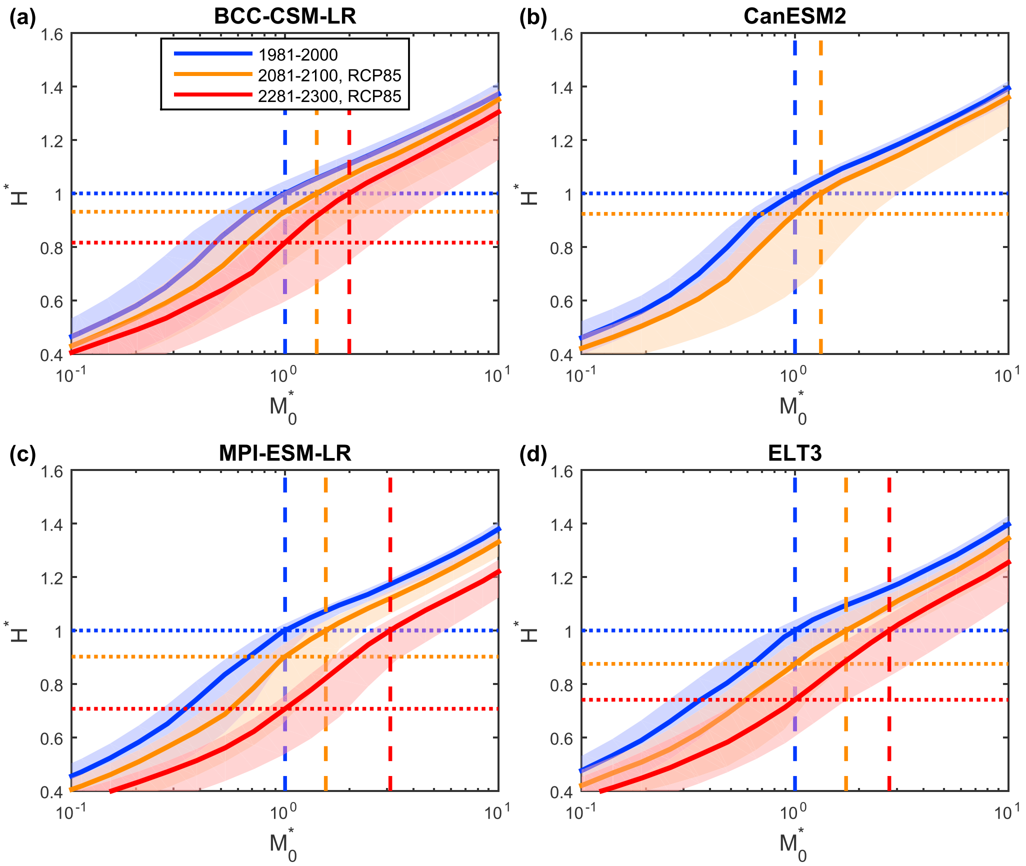

Figure 10. Same as Figure 7 but with only the Philippine region shown. The result obtained when using projection from (a) BCC-CSM-LR , (b) CanESM2, (c) MPI-ESM-LR, and (d) ELT3. Daily RCP runs for the 23rd century were not available for CanESM2.

4.2. Sensitivity Analysis

In this section we test the sensitivity of our results to the choice of GCM (section 2.2.2) and to the entrainment coefficient values applied in our volcanic plume model (section 2.3). We also briefly discuss the sensitivity of our results to the parameterization of water droplet condensation in the model and the sensitivity to variability in eruption source conditions other than the mass eruption rate.

4.2.1. Choice of GCMs

We analyze how our results differ when using an individual GCM of the ELT3 ensemble (BCC-CSM-LR, CanESM2, and MPI-ESM-LR) relative to the results when their ensemble was used. Figure 10 shows H^* as a function of M_0^* for the Philippines, for the three individual GCMs and the ensemble ELT3, and for the reference period and the late 21st and 23rd century for the RCP8.5 scenario. First, on the basis of our volcanic plume model, all GCM projections result in a decrease of H^* and an increase of the critical mass eruption rate required to reach the tropopause. For the 2081–2100 period, BCC-CSM-LR, CanESM2, and MPI-ESM-LR predict an increase by a factor of 1.35, 1.34, and 1.55 of the critical mass eruption rate required to reach the tropopause, all significant at the 99% confidence level. For the 2281–2300 period, BCC-CSM-LR and MPI-ESM-LR predict an increase by a factor of 1.99 and 3.16, respectively, both being significant again. An extended (2100–2300) RCP8.5 run of the CanESM2 model was not available.

All three GCMs we use and their ensemble (ELT3) thus show similar trends, and differences in the results do not change our conclusions. Although using an ensemble with more GCMs would make our analysis more complete statistically, we are limited by the availability of extended RCP runs with daily outputs (Table S1). For similar reasons, we also use a single run from each model. However, when comparing results using one or three runs for historical experiments for the CanESM2 and MPI-ESM-LR, we did not find any significant difference.

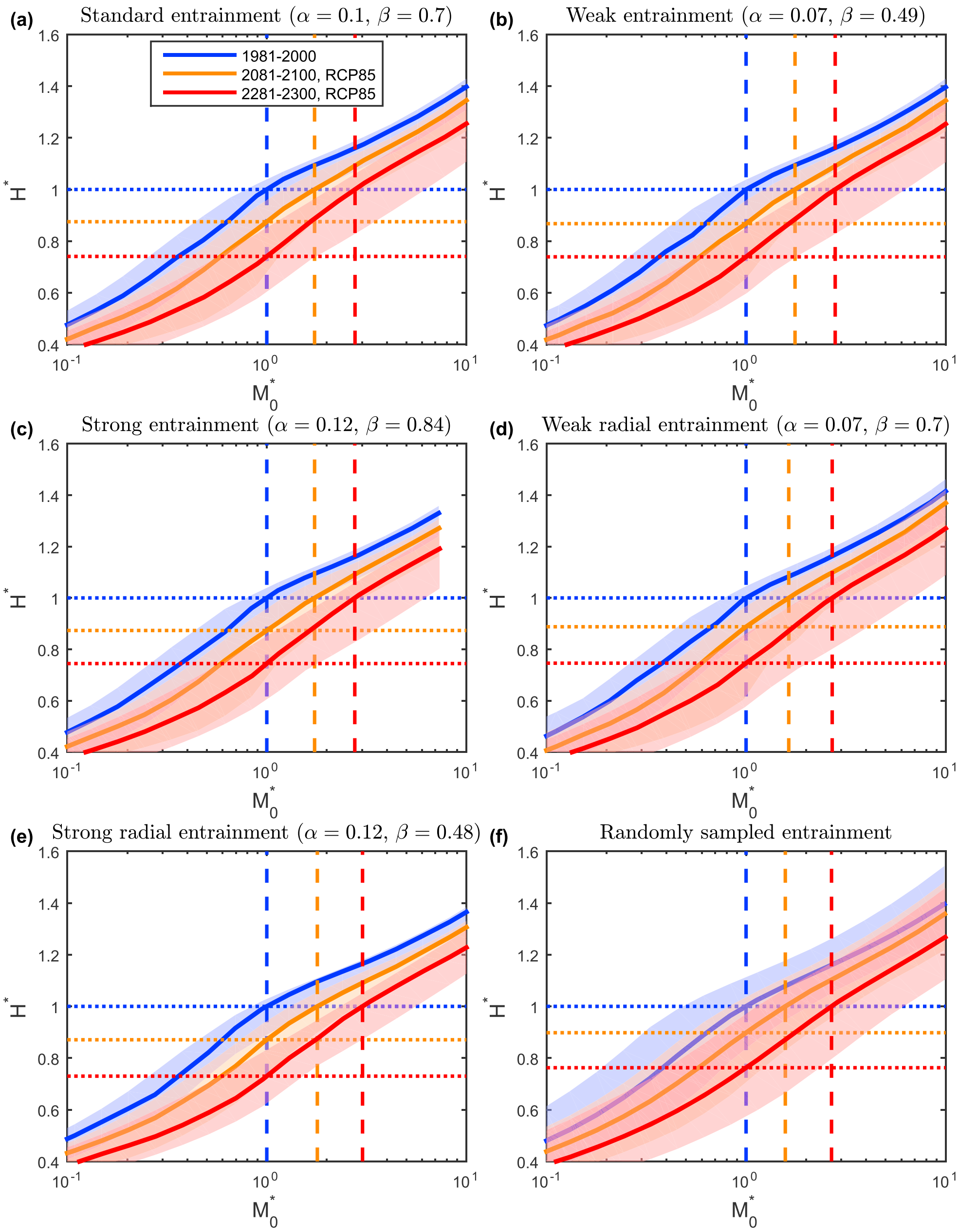

Figure 11. Same as Figure 10 but showing sensitivity of the results to entrainment rates α and β (equation (4)). Results are shown for the Philippine region using the ensemble ELT3. (a–e) We run the integral volcanic plume model with fixed values of α and β, labeled in each panel. The ratio $\frac{\beta}{\alpha}$ is equal to 7, 10, and 4 for Figures 11a–11c, 11d, and 11e, respectively. (f) We randomly sample values of α and β using a Monte Carlo simulation; we assume that α and $\frac{\beta}{\alpha}$ have normal distributions of mean 0.1 and 7 and width 0.015 and 1.5, respectively (based on a refined calibration of entrainment coefficients using the experiments of *Carazzo et al.* [2014]).

Finally, it is important to stress that two out of the three GCMs used (MPI-ESM-LR and CanESM2) are among the better performing GCMs according to the evaluation metrics tested in section 2.2.2, which gives greater confidence in our results.

4.2.2. Volcanic Plume Model Parameters

In integral volcanic plume models, the values of the entrainment coefficients α and β (equation (4)), which govern the mixing of atmosphere into the volcanic plume, must be assigned. Entrainment coefficients are identified as the main source of uncertainties on the plume height [e.g., *Costa et al.*, 2016]. To test the sensitivity of our results to entrainment coefficients, we show H^* as a function of M_0^* for the Philippines and for a RCP8.5

scenario, for the six different cases for entrainment coefficients (Figure 11). We obtain similar results when the ratio of entrainment coefficients $\frac{\beta}{\alpha}$ is kept constant ("Standard", "Weak," and "Strong" entrainment rates cases corresponding to Figures 11a–11c). When the ratio $\frac{\beta}{\alpha}$ is increased ("Weak radial entrainment rates," Figure 11d), uncertainties on H^* induced by wind are larger and changes of H^* are slightly less statistically significant. This behavior is expected as the dependence of the plume height on wind is increased when increasing $\frac{\beta}{\alpha}$. In contrast, when the ratio $\frac{\beta}{\alpha}$ is decreased ("Strong radial entrainment rate," Figure 11e), the significance of the changes slightly increases. Finally, we test the sensitivity of the results to the random choice of values for the entrainment coefficients, because entrainment coefficients depend on the plume dynamics and might vary between eruptions ("Variable entrainment rates," Figure 11f). In this case, despite the increase by $\simeq$50% of the upper bound uncertainty in H^*, the median H^* undergoes negligible change. The increase in the median critical mass eruption rate required to reach the tropopause is thus not sensitive to the value of entrainment coefficients used in the integral volcanic plume model; e.g., it varies between 2.71 and 3.02 for the six cases investigated and is always significant at the 99% level for 2281–2300.

4.2.3. Additional Factors Affecting the Height of Volcanic Plumes

The release of latent heat caused by condensation of entrained water vapor can increase volcanic plume heights, which is discussed in the supporting information (Figure S1). The impact of changes in atmospheric humidity projected by GCMs largely depends on the condensation rate λ used in the integral volcanic plume model (see section 2.3 and Table 1). For the end-member case $\lambda = 0.098$ s^{-1} (large condensation rate), the median plume height of tropospheric plume and uncertainties on plume height increase, especially in tropical regions. However, for tropical regions, the increase of the median mass eruption rate required to reach the tropopause differs negligibly from the model results that do not consider the condensation effect ($\lambda = 0$) and remain significant at the 99% level for a RCP8.5 scenario. In addition to the mass eruption rate, plume height is influenced by other source conditions. We test how the source temperature and gas content as well as the vent altitude impact our results in the supporting information (Figure S2). Among these three factors, uncertainty in the vent altitude is the main factor increasing uncertainty on plume height, but this does not affect our conclusions.

4.3. Implications for Future Volcanic Forcing

Changes in volcanic plume height and tropopause height could have significant implications for future volcanic forcing as the longevity of volcanic aerosol-radiation interactions depends strongly on whether volcanic SO_2 is injected directly into the stratosphere. The dispersal of volcanic particles also depends on plume height and wind speed and direction [e.g., *Burden et al.*, 2011]. A combined variation of all these parameters could have a significant effect on the distributions of the associated hazards. In addition, atmospheric conditions also have a significant effect on plume dynamics and, therefore, on the occurrence of associated hazardous processes (e.g., buoyant plume versus pyroclastic density currents [*Degruyter and Bonadonna*, 2013]). Although we acknowledge that these are key issues that should be explored in detail in the future, we only discuss the implications of our results for future volcanic forcing in this study.

4.3.1. Volcanic SO_2 Injection Efficiency Metric

The potential decrease of H^* by $\simeq$5–25% relative to 1981–2000 (for a RCP4.5 or RCP8.5 scenario, in the coming three centuries) has significant implications for plumes ascending to an altitude just a few kilometers above the tropopause. Although eruptions associated with these small plumes generally inject relatively moderate quantities of SO_2 into the stratosphere (Table 2), they have a significant footprint on climate [*Solomon et al.*, 2011; *Santer et al.*, 2014, 2015; *Sakai et al.*, 2016] and are more frequent than the eruptions associated with very tall plumes [*Brown et al.*, 2014]. A generic SO_2 injection efficiency metric accounting for both the quantity of SO_2 injected and the height of injection is a useful tool to further parameterize or characterize the impact of climate change on volcanic aerosol-radiation interactions. We propose this injection efficiency to be of the following form:

$$\eta_{SO_2} = \int_{M_c^*}^{\infty} \bar{n}_{SO_2} M_0^* f(M_0^*) \mathrm{d}M_0^*. \tag{5}$$

Here $\bar{n}_{SO_2}$ is the ratio of the mass of SO_2 injected by an eruption and its normalized mass eruption rate M_0^*, which is assumed to be a constant, $f(M_0^*)$ is the time-averaged frequency of an eruption of mass eruption rate M_0^*, and M_c^* is the critical normalized mass eruption rate required to reach the tropopause and is equal to 1 for the reference period by definition of M_0^*. Climate controls η_{SO_2} by governing M_c^*, whereas crustal magmatic processes might control $f(M_0^*)$ over time scales of 10^2 to 10^4 years, and magmatism related to mantle dynamics and plate tectonics enter at time scales of the order of $>10^6$ years.

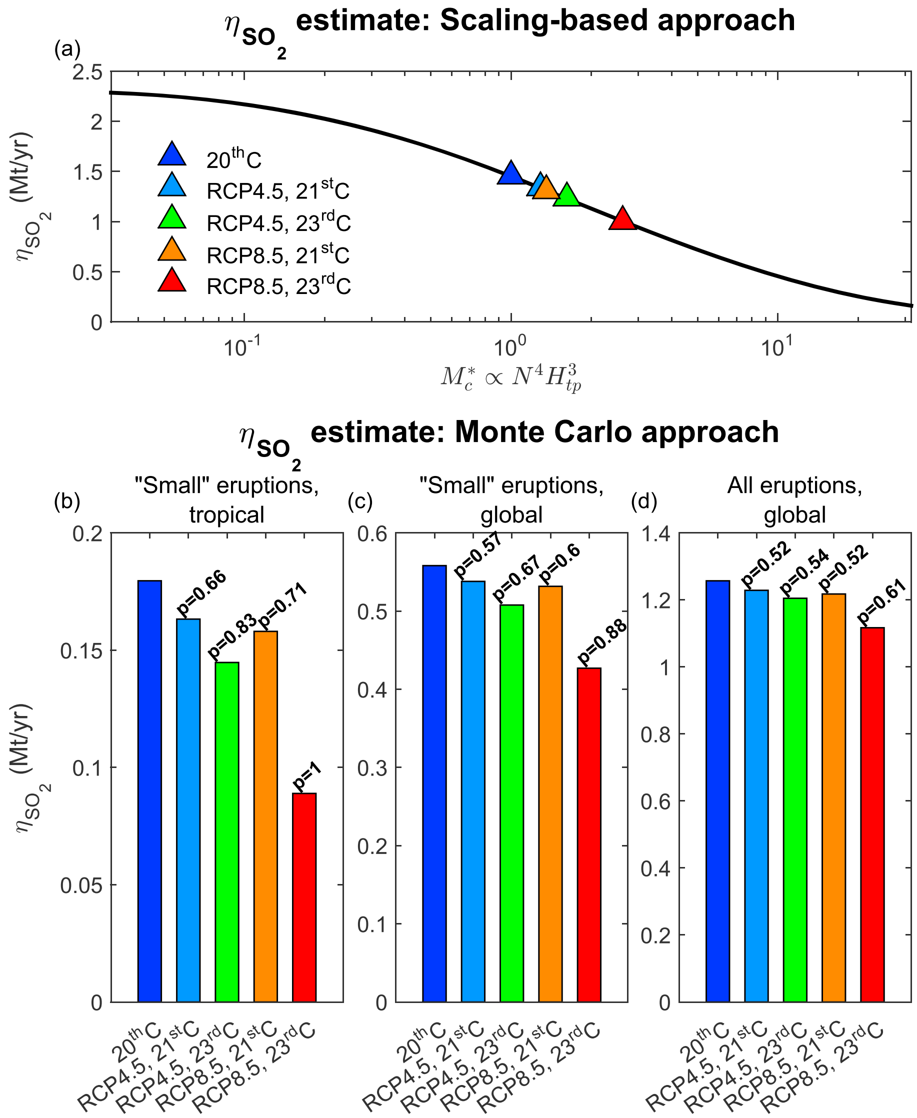

Figure 12. Projections of the volcanic SO_2 flux into the stratosphere η_{SO_2}, over a century, in Mt/yr, for 1981–2000, 2081–2100 (RCP4.5 and RCP8.5), and 2281–2300 (RCP4.5 and RCP8.5). (a) The η_{SO_2} as a function of the critical mass eruption rate M_c^* and the values of η_{SO_2} for the different scenarios estimated using the scaling-based approach of section 4.3.1 (H_{tp} is the tropopause height). (b–d) The median η_{SO_2} estimated using the Monte Carlo approach of section 4.3.2. Figure 12b shows the contribution of small (injecting less than 3 Mt of SO_2) tropical eruptions, Figure 12c the contribution of small eruptions, and Figure 12d the total flux. In Figures 12b–12d, for future periods, the probability p for η_{SO_2} to be lower than under the reference climate is indicated.

To estimate η_{SO_2} for the reference period, we take $\bar{n}_{SO_2}$ to be the average value of the ratio of the mass of SO_2 injected by an eruption to its normalized mass eruption rate M_0^* in the *Carn et al.* [2016] data set. To estimate $f(M_0^*)$, we use the *Carn et al.* [2016] data set for the frequent eruptions injecting less than $\simeq$3 Mt of SO_2 that contribute to aerosol background. We use the *Sigl et al.* [2015] data set for intermittent events injecting more than $\simeq$3 Mt of SO_2. Figure S3 shows the distribution of erupted mass of SO_2 from both data sets, to which we fit $f(M_0^*)$ using a Kernel distribution. Figure 12a shows the estimated values of η_{SO_2} as a function of M_c^*. Using M_c^*=1, we find η_{SO_2} = 1.45 Mt/yr for the reference period, which is close to the value of 1.23 Mt/yr estimated in Figure 9 using the *Carn et al.* [2016] data set only. To estimate η_{SO_2} for an arbitrary period, we use equation (1). Let r_T be the ratio of the tropopause height of the period considered to the tropopause height of the reference period. Let r_N be the ratio of the Brunt-Väisälä frequencies for the same periods. Then, using equation (1), $M_c^* = r_T^4 r_N^3$. Figure 12 shows this scaling-based estimate of η_{SO_2} for RCP4.5 and RCP8.5 scenarios. Using average changes in tropical tropopause height and tropospheric temperature lapse rate to calculate M_c^*, we find

η_{SO_2}=1.34 Mt/yr and η_{SO_2}=1.31 Mt/yr for the late 21st century for the RCP4.5 and RCP8.5 scenarios, respectively, and η_{SO_2}=1.23 Mt/yr and η_{SO_2}=1.0 Mt/yr for the late 23rd century for the same scenarios (Figure 12a). Relative decreases in the volcanic injection of SO_2 into the stratosphere using this simple, scaling-based approach are thus remarkably close to the ones estimated in Figure 9.

4.3.2. Magnitude and Likelihood of Projected Changes in Volcanic SO_2 Fluxes Into the Stratosphere

Estimates of η_{SO_2} either on the basis of the scaling-based approach of section 4.3.1 or from Figure 9 rely on several assumptions. In particular, estimates from Figure 9 assume that (i) the 1980–2015 sequence of eruptions will be repeated in the future; (ii) all volcanic SO_2 is injected at the maximum plume altitude; and (iii) the plume altitude is the median altitude for the considered period and RCP scenario. In addition, we use a steady state plume model, which cannot account for the potential additional transport of SO_2 across the tropopause by atmospheric circulation [e.g., *Bourassa et al.*, 2012] or by natural convection after absorption and warming [e.g., *de Laat et al.*, 2012].

In a preliminary effort to relax some of these assumptions, we use a Monte Carlo method to estimate future stratospheric injection of volcanic SO_2 over a century, for a specified time period and forcing scenario. For one simulation, we randomly sample 36,525 days (100 years) in the 1980–2015 period, which is the longest period with available plume height and SO_2 loading for most eruptions. For each day corresponding to an eruption in the *Carn et al.* [2016] data set injecting less than 3 Mt of SO_2, we assume that an eruption occurs with the following characteristics:

1. The region and vent altitude is the same as for the original eruption.
2. The mass eruption rate is $10^{\psi} \times M_{Carn}$ where M_{Carn} is the mass eruption rate of the original eruption and ψ is a random number between −0.3 and 0.3. Since $10^{0.3} \simeq 2$, the resulting mass eruption rate is within a factor of 2 of the mass eruption rate of the original eruption. This approach enables us to randomize the mass eruption rate, while preserving its order of magnitude such that the distribution of mass eruption rates is similar to the one inferred for the 1980–2015 period.
3. The mass of SO_2 is $10^{\phi} \times MSO2_{Carn}$ where $MSO2_{Carn}$ is the mass of SO_2 of the original eruption and ϕ is a random number between −0.3 and 0.3, where the choice of random number range is based on the same argument as for the mass eruption rate.
4. Atmospheric conditions correspond to a day randomly sampled from the GCM ensemble, for the specified period and scenario.
5. The SO_2 is uniformly distributed between H_b and $2H - H_b$ where H is the maximum plume altitude and H_b the altitude of neutral buoyancy of the plume. This approach is approximately equivalent to distributing the SO_2 over a layer of height 30–50% of the maximum height. For a steady plume and in the absence of additional vertical transport by atmospheric winds or thermal convection, we would have distributed the SO_2 in a layer of thickness $H-H_b$. Here we arbitrarily double this thickness to explore a larger vertical spread of the SO_2 due to unsteadiness and spreading mechanisms mentioned above. The chosen layer thickness is coherent with uncertainties on observed plume height shown in Figure 8, which are due to a large extent to unsteadiness of the eruption or uncertainties related to vertical transport of the plume.

Last, we randomly sample a 100 year period in the *Sigl et al.* [2015] data set from which we excluded eruptions injecting less than 3 Mt of SO_2. We assume that corresponding sampled eruptions inject SO_2 directly into the stratosphere, regardless of atmospheric conditions.

We perform 300 Monte Carlo simulations of 100 years of volcanic eruptions for the late 21st and late 23rd centuries for RCP4.5 and RCP8.5 scenarios, as well as for the reference period. Results are not sensible to the number of simulations performed for more than ≃100 simulations. Figure 12 shows the median flux of SO_2 into the stratosphere η_{SO_2} (d) as well as the median global (c) and tropical (b) flux of volcanic SO_2 into the stratosphere due to small eruptions only (i.e., the ones injecting less than ≃3 Mt of SO_2 that are sampled from the *Carn et al.* [2016] data set). The probability for projected stratospheric fluxes of future time periods to be smaller than fluxes for the reference period is also reported on each panel.

Figure 12c shows that the flux of SO_2 into the stratosphere related to small eruptions may decrease by ≃5–25% for a RCP4.5 or RCP8.5 scenario depending on the period considered. A decrease is “likely” (66 to 90% probability, using the IPCC AR5 likelihood scale [*Mastrandrea et al.*, 2010]) by the 23rd century but “about as likely as not” (33 to 66% probability) for the 21st century due to large uncertainties related to future eruptive conditions. Projected decreases of the tropical flux of SO_2 carried by small eruptions (Figure 12b) are larger (≃10–50%), and “likely” (66 to 90% probability) to “very likely” (≥90%) . However, Figure 12d shows that the total flux, including the contribution from large eruptions, would undergo a smaller decrease (≃2–12%) that would be "about as likely as not" due to the large simulated variability in volcanic SO_2 fluxes when including contribution from all eruptions. Reductions are even smaller and less likely for a RCP2.6 scenario (not shown).

To summarize, our results suggest that global warming may significantly decrease the background volcanic flux of SO_2 into the stratosphere sustained by small ($\lesssim$3 Mt of SO_2) and frequent (compared to the rate of decay of stratospheric sulfate aerosols) stratospheric injections. However, the effect on the total flux of SO_2 into the stratosphere is small because of the contributions of large ($\gtrsim$3 Mt of SO_2) and infrequent (compared to the rate of decay of stratospheric sulfate aerosols) events. As a final remark on this result, our view may be conservative because we assume that large eruptions inject SO_2 into the stratosphere regardless of climate, which is not the case at least for basaltic eruptions such as the 1783–1784 eruptions of Laki [*Thordarson and Self*, 2003] as shown in Figure 8.

Critically, our estimates of a decrease of the flux of volcanic SO_2 into the stratosphere challenges the use of steady volcanic forcing for climate projections in two ways. First, our results suggest a new positive feedback between climate and volcanic aerosol-radiation interaction: (i) global warming decreases the frequency of eruptions with stratospheric injections; (ii) less frequent stratospheric volcanic injections result in a decrease of the long-term average sulfate aerosol concentration in the stratosphere and thus of the albedo of the atmosphere; and (iii) a reduced atmospheric albedo will enhance global warming. Assuming a long-term average volcanic forcing of small eruptions (VEI $\leqslant 5$) of order of magnitude -0.1 W m $^{-2}$ [*Solomon et al.*, 2011; *Sakai et al.*, 2016] and that the relative variations in this average would be of the same order of magnitude as change in the average volcanic SO_2 flux into the stratosphere, the order of magnitude of this feedback would be 10^{-2} W m^{-2}/°C. It may thus make a negligible contribution to global warming rate, although we note that the order of magnitude of projected changes in stratospheric SO_2 flux is comparable to the increase in volcanic stratospheric SO_2 since 2002 which has been argued to contribute to overestimates of global warming rate by GCMs [e.g., *Solomon et al.*, 2011; *Santer et al.*, 2014; *Sakai et al.*, 2016] The proposed feedback may also prove important for understanding the evolution of volcanic aerosol forcing in the future, as well as the overall impact of Earth's climate on the distribution of volcanic inputs in the atmosphere. Second, our statistical analyses suggest that for a given climate, the average flux of volcanic SO_2 into the stratosphere over a century may vary by a factor of ≃5–10, which would likely have important consequences for forcing related to volcanic aerosol-radiation interactions and may increase uncertainties in future climate projections.

4.4. Limitations and Potential Improvements: Beyond a Binary View of Volcanic Aerosol Forcing Sensitivity to Plume Height

The discussion of our results is grounded in the assumption that only stratospheric aerosols exert a significant influence on global climate. Although this is a good first approximation, the shift in impact between a tropospheric and stratospheric injection of SO_2 is not as abrupt. The following considerations enter the full picture of volcanic forcing:

1. For stratospheric plumes, aerosol-radiation interactions are sensitive to the plume height, although most sensitivity studies focus on the impact of the eruption season and latitude. *Stoffel et al.* [2015] test the sensitivity of climate response to plume height for the Samalas 1257 eruption and report larger aerosol optical depth and 40°N–90°N land temperature anomalies for an upper stratospheric injection (36–43 km) compared to a lower stratospheric injection (22–26 km), with differences by up to a factor of ≃2 depending on the season. A sensitivity study for high-latitude eruptions using a GCM coupled with a stratospheric chemistry/aerosol microphysics module suggests similar effects (M. Toohey, personal communication, 2016). For high-latitude eruptions, aerosol clouds issued from stratospheric plumes smaller than the tropical tropopause spread along constant potential temperature surface and may thus cross the tropopause and be scavenged at midlatitudes [*Holton et al.*, 1995]. *Carn et al.* [2016], on the basis of satellite measurements, also show that the *e*-folding time for SO_2 removal increases with the plume height and suggest that H^* is the main parameter controlling the longevity of SO_2. Greater longevity for SO_2 may lead to a slower aerosol production and to a reduced but longer-lasting peak of volcanic aerosol-radiation interactions [*Timmreck*, 2012]. Thus, the decrease of H^* for large stratospheric plumes (Figures 7 and 9) might have important consequences for future radiative forcing even if they are not shifted below the tropopause.
2. Tropospheric eruptive plumes also impact climate by increasing cloud condensation nuclei concentrations and, in turn, cloud reflectivity (aerosol-cloud interactions). For example, during the Bárðarbunga 2014–2015 eruption (Iceland), *McCoy and Hartmann* [2015] report increases of up to 2 W m^{-2} in the

reflected solar radiation, over the North Atlantic. *Schmidt et al.* [2012] estimate that the long-term average volcanic aerosol-cloud interactions forcing is $\simeq -0.3$ to -1.6 W m^{-2}, depending on the background aerosol concentrations). As aerosol and nucleated cloud radiative properties depend on the height of injection of volcanic SO_2 in the troposphere [*Schmidt et al.*, 2016], volcanic aerosol-cloud interactions may also depend on the height of volcanic plumes. As a result, a larger injection of volcanic SO_2 into the troposphere and the decrease of the height of tropospheric plumes (Figure 8) may increase future volcanic aerosol-cloud interactions forcing, although the projected increase in volcanic SO_2 flux into the troposphere is small ($\simeq 0-5\%$, estimated from Figure 12c and tropospheric flux estimates from *Halmer et al.* [2002] and *Carn et al.* [2016]).

3. An injection of SO_2 directly into the stratosphere may not be necessary for the SO_2 or sulfur aerosol to reach the stratosphere and result in significant aerosol-radiation interactions. Upper tropospheric volcanic sulfur gases or aerosols may be transported to some extent through the tropopause by atmospheric circulation [*Bourassa et al.*, 2012, 2013; *Clarisse et al.*, 2014] or by convection driven as a result of absorption of Earth and Sun radiation, which has been suggested for the Black Sunday fire [*de Laat et al.*, 2012].
4. Even when a volcanic eruption produces a stable plume, part of the erupted material may collapse to form pyroclastic flows [*Carazzo and Jellinek*, 2012]. Part of the SO_2 lost to pyroclastic flows may, however, be entrained into coignimbrite columns [*Woods and Wohletz*, 1991]. Although the height reached by coignimbrite plumes are typically lower than the main plinian column with which they are associated, they may transport SO_2 into the stratosphere for very large eruptions such as Tambora in 1815 or Pinatubo in 1991 [*Herzog and Graf*, 2010]. Such effects would not be captured by the model used in this study.

Different modeling approaches can be applied to tackle some of these four limitations. For example, in order to estimate changes in volcanic aerosol-radiation interactions, our plume model can provide SO_2 altitude and loading to an idealized volcanic aerosol model, such as Easy Volcanic Aerosol [*Toohey et al.*, 2016b], or to a GCM coupled with a stratospheric chemistry/aerosols microphysics module, such as MAECHAM5-HAM [e.g., *Toohey et al.*, 2011]. The use of a three-dimensional plume model instead of an integral volcanic plume model may enable to better account for the complexity of the flows resulting from volcanic eruptions, such as coignimbrite plumes.

As a final note to this discussion, global warming may impact volcanic aerosol forcing via mechanisms different than the one proposed here. For example, the gradual melting of continental snow and ice cover implies that future eruptions are less likely to melt and entrain surface water into the eruption plume, which may affect both the probability of collapse of a plume [*Koyaguchi and Woods*, 1996] and the radiative forcing of the eruption [*LeGrande et al.*, 2016]. Changes in atmospheric circulation may affect the distribution and *e*-folding time of stratospheric aerosols [e.g., *McLandress and Shepherd*, 2009; *Jones et al.*, 2016], and changes in water vapor may affect the aerosol size and thus their radiative properties and *e*-folding time [e.g., *Gettelman et al.*, 2010]. Finally, a number of studies show that eruption frequency is impacted by continental ice sheets, alpine glacier, or sea level change [e.g., *Hall*, 1982; *McGuire et al.*, 1997; *Jellinek et al.*, 2004]. The response of volcanic aerosol forcing to these combined effects may improve our understanding of the evolution of volcanic aerosol forcing. Beyond sulfur aerosol, our work has implications for the lifetime of other volcanic forcing agent in the atmosphere such as fine volcanic ash which has been suggested to amplify aerosol forcing by 20% for at least 3 months following the Kelut 2014 eruption [*Vernier et al.*, 2016].

5. Conclusions

In this study, we investigate whether the ongoing global warming, driven by anthropogenic greenhouse gas emissions, will shift volcanic eruption plume height relative to the tropopause height. We compute volcanic plume heights using an integral volcanic plume model. Atmospheric conditions are obtained from an ensemble of GCM runs for historical and RCP experiments.

We find that the critical mass eruption rate required to reach the tropopause will increase as a consequence of (i) a decrease in the heights of tropospheric plumes driven by a decrease in the tropospheric temperature lapse rate and (ii) an increase in the tropopause height. This result is independent of the choice of GCMs and insensitive to parameterizations for the volcanic plume model. Depending on the latitudinal zone, RCP scenario, and time period considered, the critical mass eruption rate increases by up to a factor of 2.8 relative to the late twentieth century. This increase is significant in tropical regions for a RCP4.5 scenario and all tested regions for a RCP8.5 scenario. This result implies that eruptions rising a few kilometers above the tropopause under current climate conditions may be shifted to the stratosphere in the future. As a consequence, we estimate that the flux of SO_2 into the stratosphere associated to small ($\leq$3 Mt of SO_2) frequent (compared to the rate of decay of stratospheric sulfate aerosols) eruptions would likely decrease by $\simeq$5–25% over the next three centuries, for a RCP4.5 or RCP8.5 scenario. The amplitude and likelihood of such decrease is more pronounced for tropical injections. Due to the contribution of large ($\geq$3 Mt of SO_2) infrequent (compared to the rate of decay of stratospheric volcanic aerosol) eruptions, and to large uncertainties in future eruptive source conditions, the total flux of volcanic SO_2 into the stratosphere is projected to decrease by $\simeq$2–12%, with the likelihood of such decrease being weak. Finally, our results challenge the popular use of steady volcanic radiative forcing in climate projections for the coming centuries. Instead, our work suggests that greenhouse gas-driven climate change will result in less cooling from volcanic eruptions, potentially resulting in a positive feedback. The expected amplitude for this feedback is small, although it has been argued that the increase in stratospheric SO_2 injections since 2002, the amplitudes of which are comparable to the decrease projected in our study, has contributed to the overestimation of global warming rate by GCMs [e.g., *Solomon et al.*, 2011; *Santer et al.*, 2014]. While processes linking eruptive source conditions to the distribution of volcanic SO_2 are neglected in past GCM experiments on volcanic forcing [e.g., *Stenchikov et al.*, 2006; *Driscoll et al.*, 2012] and in the next Model Intercomparison Project on the climatic response to Volcanic forcing [*Zanchettin et al.*, 2016], we demonstrate that such processes may prove critical to the understanding of past and future volcanic forcing.

Acknowledgments
The authors warmly thank Anja Schmidt, Alan Robock, Jim Haywood, and Benjamin Edwards who organized the Climate-Volcano Feedbacks sessions VS32/33 at the International Union of Geodesy and Geophysics 2016, which motivated this work. This work benefited from very useful discussions with Matthew Toohey and all participants of the Volcanic Impacts on Climate and Society 2016 workshop. We thank the Editor, Associate Editor, and three anonymous reviewers for their thorough comments and suggestions which greatly improved the original manuscript. Thomas J. Aubry acknowledges funding from the University of British Columbia through a Four Year Fellowship. Thomas J. Aubry, A. Mark Jellinek and Valentina Radić were supported by Natural Sciences and Engineering Research Council of Canada during completion of this work. Costanza Bonadonna was supported by the Swiss National Science Foundation (project 200021_156255). We acknowledge the World Climate Research Programme's Working Group on Coupled Modeling, which is responsible for CMIP, and we thank the climate modeling groups for producing and making available their model output. We thank the NOAA/OAR/ESRL/PSD and the ECMWF for making reanalysis data available. We thank Simon A. Carn and the National Aeronautics and Space Administration Goddard Earth Sciences Data and Information Services Center for making available the Multi-Satellite Volcanic Sulfur Dioxide Database Long-Term. We acknowledge the Smithsonian Institution Global Volcanism Program for compiling the Holocene volcanoes database. We thank the Laboratory of Computer and Information Science for making the SOM toolbox v2.0 freely available on http://www.cis.hut.fi/projects/somtoolbox/.

References

Bonadonna, C., M. Pistolesi, R. Cioni, W. Degruyter, M. Elissondo, and V. Baumann (2015), Dynamics of wind-affected volcanic plumes: The example of the 2011 Cordón Caulle eruption, Chile, *J. Geophys. Res. Solid Earth*, *120*, 2242–2261, doi:10.1002/2014JB011478.

Bourassa, A. E., A. Robock, W. J. Randel, T. Deshler, L. A. Rieger, N. D. Lloyd, E. T. Llewellyn, and D. A. Degenstein (2012), Large volcanic aerosol load in the stratosphere linked to Asian monsoon transport, *Science*, *337*(6090), 78–81, doi:10.1126/science.1219371.

Bourassa, A. E., A. Robock, W. J. Randel, T. Deshler, L. A. Rieger, N. D. Lloyd, E. Llewellyn, and D. A. Degenstein (2013), Response to comments on "Large volcanic aerosol load in the stratosphere linked to Asian monsoon transport", *Science*, *339*(6120), 647–647, doi:10.1126/science.1227961.

Brown, S. K., et al. (2014), Characterisation of the Quaternary eruption record: Analysis of the large magnitude explosive volcanic eruptions (LaMEVE) database, *J. Appl. Volcanol.*, *3*(1), 1–22, doi:10.1186/2191-5040-3-5.

Brühl, C., J. Lelieveld, H. Tost, M. Höpfner, and N. Glatthor (2015), Stratospheric sulfur and its implications for radiative forcing simulated by the chemistry climate model EMAC, *J. Geophys. Res. Atmos.*, *120*, 2103–2118, doi:10.1002/2014JD022430.

Burden, R. E., J. C. Phillips, and T. K. Hincks (2011), Estimating volcanic plume heights from depositional clast size, *J. Geophys. Res.*, *116*, B11206, doi:10.1029/2011JB008548.

Bursik, M. (2001), Effect of wind on the rise height of volcanic plumes, *Geophys. Res. Lett.*, *28*, 3821–3824, doi:10.1029/2001GL013393.

Carazzo, G., and A. M. Jellinek (2012), A new view of the dynamics, stability and longevity of volcanic clouds, *325–326*, 39–51, doi:10.1016/j.epsl.2012.01.025.

Carazzo, G., F. Girault, T. J. Aubry, H. Bouquerel, and E. Kaminski (2014), Laboratory experiments of forced plumes in a density-stratified crossflow and implications for volcanic plumes, *Geophys. Res. Lett.*, *41*, 8759–8766, doi:10.1002/2014GL061887.

Carn, S., L. Clarisse, and A. Prata (2016), Multi-decadal satellite measurements of global volcanic degassing, *J. Volcanol. Geotherm. Res.*, *311*, 99–134, doi:10.1016/j.jvolgeores.2016.01.002.

Chylek, P., J. Li, M. Dubey, M. Wang, and G. Lesins (2011), Observed and model simulated 20th century Arctic temperature variability: Canadian Earth System Model CanESM2, *Atmos. Chem. Phys. Discuss.*, *11*(8), 22,893–22,907, doi:10.5194/acpd-11-22893-2011.

Clarisse, L., P.-F. Coheur, N. Theys, D. Hurtmans, and C. Clerbaux (2014), The 2011 Nabro eruption, a SO_2 plume height analysis using IASI measurements, *Atmos. Chem. Phys.*, *14*(6), 3095–3111, doi:10.5194/acp-14-3095-2014.

Collins, M., et al. (2013), *Long-Term Climate Change: Projections, Commitments and Irreversibility*, book section 12, pp. 1029–1136, Cambridge Univ. Press, Cambridge, U. K., and New York, doi:10.1017/CBO9781107415324.024.

Costa, A., et al. (2016), Results of the eruptive column model inter-comparison study, *J. Volcanol. Geotherm. Res.*, *326*, 2–25, doi:10.1016/j.jvolgeores.2016.01.017.

de Laat, A. T. J., D. C. Stein Zweers, R. Boers, and O. N. E. Tuinder (2012), A solar escalator: Observational evidence of the self-lifting of smoke and aerosols by absorption of solar radiation in the February 2009 Australian Black Saturday plume, *J. Geophys. Res.*, *117*, D04204, doi:10.1029/2011JD017016.

Degruyter, W., and C. Bonadonna (2012), Improving on mass flow rate estimates of volcanic eruptions, *Geophys. Res. Lett.*, *39*, L16308, doi:10.1029/2012GL052566.

Degruyter, W., and C. Bonadonna (2013), Impact of wind on the condition for column collapse of volcanic plumes, *Earth Planet. Sci. Lett.*, *377*, 218–226, doi:10.1016/j.epsl.2013.06.041.

Driscoll, S., A. Bozzo, L. J. Gray, A. Robock, and G. Stenchikov (2012), Coupled Model Intercomparison Project 5 (CMIP5) simulations of climate following volcanic eruptions, *J. Geophys. Res.*, *117*, D17105, doi:10.1029/2012JD017607.

Flato, G., et al. (2013), *Evaluation of Climate Models*, book section 9, pp. 741–866, Cambridge Univ. Press, Cambridge, U. K., and New York, doi:10.1017/CBO9781107415324.020.

Folch, A., A. Costa, and G. Macedonio (2016), FPLUME-1.0: An integral volcanic plume model accounting for ash aggregation, *Geoscientific Model Development*, *9*(1), 431, doi:10.5194/gmd-9-431-2016.

Fromm, M., G. Nedoluha, and Z. Charvát (2013), Comment on "Large volcanic aerosol load in the stratosphere linked to Asian monsoon transport", *Science*, *339*(6120), 647–647, doi:10.1126/science.1228605.

Fu, Q., S. Manabe, and C. M. Johanson (2011), On the warming in the tropical upper troposphere: Models versus observations, *Geophys. Res. Lett.*, *38*, L15704, doi:10.1029/2011GL048101.

Gettelman, A., et al. (2010), Multimodel assessment of the upper troposphere and lower stratosphere: Tropics and global trends, *J. Geophys. Res.*, *115*, D00M08, doi:10.1029/2009JD013638.

Giorgetta, M. A., et al. (2013), Climate and carbon cycle changes from 1850 to 2100 in MPI-ESM simulations for the Coupled Model Intercomparison Project phase 5, *J. Adv. Model. Earth Syst.*, *5*(3), 572–597, doi:10.1002/jame.20038.

Glaze, L. S., S. M. Baloga, and L. Wilson (1997), Transport of atmospheric water vapor by volcanic eruption columns, *J. Geophys. Res.*, *102*(D5), 6099–6108, doi:10.1029/96JD03125.

Glaze, L. S., S. Self, A. Schmidt, and S. J. Hunter (2015), Assessing eruption column height in ancient flood basalt eruptions, *Earth Planet. Sci. Lett.*, doi:10.1016/j.epsl.2014.07.043, in press.

Gleckler, P. J., K. E. Taylor, and C. Doutriaux (2008), Performance metrics for climate models, *J. Geophys. Res.*, *113*, D06104, doi:10.1029/2007JD008972.

Guo, S., G. J. S. Bluth, W. I. Rose, I. M. Watson, and A. J. Prata (2004), Re-evaluation of SO_2 release of the 15 June 1991 Pinatubo eruption using ultraviolet and infrared satellite sensors, *Geochem. Geophys. Geosyst.*, *5*, Q04001, doi:10.1029/2003GC000654.

Hall, K. (1982), Rapid deglaciation as an initiator of volcanic activity: An hypothesis, *Earth Surf. Process. Landforms*, *7*(1), 45–51, doi:10.1002/esp.3290070106.

Halmer, M., H.-U. Schmincke, and H.-F. Graf (2002), The annual volcanic gas input into the atmosphere, in particular into the stratosphere: A global data set for the past 100 years, *J. Volcanol. Geotherm. Res.*, *115*(3–4), 511–528, doi:10.1016/S0377-0273(01)00318-3.

Hartmann, D., et al. (2013), *Observations: Atmosphere and Surface*, book section 2, pp. 159–254, Cambridge Univ. Press, Cambridge, U. K., and New York, doi:10.1017/CBO9781107415324.008.

Haywood, J. M., A. Jones, and G. S. Jones (2014), The impact of volcanic eruptions in the period 2000–2013 on global mean temperature trends evaluated in the HadGEM2-ES climate model, *Atmos. Sci. Lett.*, *15*(2), 92–96, doi:10.1002/asl2.471.

Herzog, M., and H.-F. Graf (2010), Applying the three-dimensional model ATHAM to volcanic plumes: Dynamic of large co-ignimbrite eruptions and associated injection heights for volcanic gases, *Geophys. Res. Lett.*, *37*, L19807, doi:10.1029/2010GL044986.

Hewett, T., J. Fay, and D. Hoult (1971), Laboratory experiments of smokestack plumes in a stable atmosphere, *Atmos. Environ.*, *5*, 767–789.

Holton, J. R., P. H. Haynes, M. E. McIntyre, A. R. Douglass, R. B. Rood, and L. Pfister (1995), Stratosphere-troposphere exchange, *Rev. Geophys.*, *33*(4), 403–439, doi:10.1029/95RG02097.

Iles, C., and G. Hegerl (2015), Systematic change in global patterns of streamflow following volcanic eruptions, *Nat. Geosci.*, *8*(11), 838–842, doi:10.1038/ngeo2545.

Jellinek, A. M., M. Manga, and M. O. Saar (2004), Did melting glaciers cause volcanic eruptions in eastern California? Probing the mechanics of dike formation, *J. Geophys. Res.*, *109*, B09206, doi:10.1029/2004JB002978.

Jones, A. C., J. M. Haywood, A. Jones, and V. Aquila (2016), Sensitivity of volcanic aerosol dispersion to meteorological conditions: A Pinatubo case study, *J. Geophys. Res. Atmos.*, *121*, 6892–6908, doi:10.1002/2016JD025001.

Kalnay, E., et al. (1996), The NCEP/NCAR 40-year reanalysis project, *Bull. Am. Meteorol. Soc.*, *77*(3), 437–471, doi:10.1175/1520-0477(1996)077.

Kohonen, T. (1982), Self-organized formation of topologically correct feature maps, *Biol. Cybernetics*, *43*(1), 59–69, doi:10.1007/BF00337288.

Koyaguchi, T., and A. W. Woods (1996), On the formation of eruption columns following explosive mixing of magma and surface-water, *J. Geophys. Res.*, *101*(B3), 5561–5574, doi:10.1029/95JB01687.

LeGrande, A. N., K. Tsigaridis, and S. E. Bauer (2016), Role of atmospheric chemistry in the climate impacts of stratospheric volcanic injections, *Nat. Geosci.*, *9*, 652–655, doi:10.1038/ngeo2771.

Mastin, L. (2014), Testing the accuracy of a 1-D volcanic plume model in estimating mass eruption rate, *J. Geophys. Res. Atmos.*, *119*, 2474–2495, doi:10.1002/2013JD020604.

Mastin, L., et al. (2009), A multidisciplinary effort to assign realistic source parameters to models of volcanic ash-cloud transport and dispersion during eruptions, *J. Volcanol. Geotherm. Res.*, *186*(1), 10–21, doi:10.1016/j.jvolgeores.2009.01.008.

Mastrandrea, M. D., et al. (2010), Guidance note for lead authors of the IPCC fifth assessment report on consistent treatment of uncertainties. Intergovernmental Panel on Climate Change (IPCC). [Available at https://www.ipcc.ch/pdf/supporting-material/uncertainty-guidance-note.pdf, accessed 8 November 2016].

McCoy, D. T., and D. L. Hartmann (2015), Observations of a substantial cloud-aerosol indirect effect during the 2014–2015 Bárðarbunga-Veiðivötn fissure eruption in Iceland, *Geophys. Res. Lett.*, *42*, 10,409–10,414, doi:10.1002/2015GL067070.

McGregor, S., and A. Timmermann (2010), The effect of explosive tropical volcanism on ENSO, *J. Clim.*, *24*, 2178–2191, doi:10.1175/2010JCLI3990.1.

McGuire, W. J., R. J. Howarth, C. R. Firth, A. R. Solow, A. D. Pullen, S. J. Saunders, I. S. Stewart, and C. Vita-Finzi (1997), Correlation between rate of sea-level change and frequency of explosive volcanism in the Mediterranean, *Nature*, *389*(6650), 473–476, doi:10.1038/38998.

McLandress, C., and T. G. Shepherd (2009), Simulated anthropogenic changes in the Brewer-Dobson circulation, including its extension to high latitudes, *J. Clim.*, *22*(6), 1516–1540, doi:10.1175/2008JCLI2679.1.

Mignot, J., M. Khodri, C. Frankignoul, and J. Servonnat (2011), Volcanic impact on the Atlantic ocean over the last millennium, *Clim. Past*, *7*(4), 1439–1455, doi:10.5194/cp-7-1439-2011.

Mills, M. J., et al. (2016), Global volcanic aerosol properties derived from emissions, 1990–2014, using CESM1 (WACCM), *J. Geophys. Res. Atmos.*, *121*, 2332–2348, doi:10.1002/2015JD024290.

Mitchell, D., P. Thorne, P. Stott, and L. Gray (2013), Revisiting the controversial issue of tropical tropospheric temperature trends, *Geophys. Res. Lett.*, *40*, 2801–2806, doi:10.1002/grl.50465.

Morton, B. (1957), Buoyant plumes in a moist atmosphere, *J. Fluid Mech.*, *2*(02), 127–144, doi:10.1017/S0022112057000038.

Morton, B. R., G. Taylor, and J. S. Turner (1956), Turbulent gravitational convection from maintained and instantaneous sources, *Proc. R. Soc. A*, *234*(1196), 1–23, doi:10.1098/rspa.1956.0011.

Newhall, C. G., and S. Self (1982), The Volcanic Explosivity Index (VEI): An estimate of explosive magnitude for historical volcanism, *J. Geophys. Res.*, *87*, 1231–1238, doi:10.1029/JC087iC02p01231.

Prata, A., S. Carn, A. Stohl, and J. Kerkmann (2007), Long range transport and fate of a stratospheric volcanic cloud from Soufrière Hills volcano, Montserrat, *Atmos. Chem. Phys.*, *7*(19), 5093–5103, doi:10.5194/acp-7-5093-2007.

Radić, V., A. J. Cannon, B. Menounos, and N. Gi (2015), Future changes in autumn atmospheric river events in British Columbia, Canada, as projected by CMIP5 global climate models, *J. Geophys. Res. Atmos.*, *120*, 9279–9302, doi:10.1002/2015JD023279.

Ridley, D. A., et al. (2014), Total volcanic stratospheric aerosol optical depths and implications for global climate change, *Geophys. Res. Lett.*, *41*, 7763–7769, doi:10.1002/2014GL061541.

Rieger, L. A., A. E. Bourassa, and D. A. Degenstein (2015), Merging the OSIRIS and SAGE II stratospheric aerosol records, *J. Geophys. Res. Atmos.*, *120*, 8890–8904, doi:10.1002/2015JD023133.

Robock, A. (2000), Volcanic eruptions and climate, *Rev. Geophys.*, *38*, 191–219, doi:10.1029/1998RG000054.

Rymer, H. (2015), *The Encyclopedia of Volcanoes*, 2nd ed., pp. 895–896, Academic Press, doi:10.1016/B978-0-12-385938-9.02009-5. [Available at http://www.sciencedirect.com/science/book/9780123859389 accessed on 8 November 2016.]

Sakai, T., O. Uchino, T. Nagai, B. Liley, I. Morino, and T. Fujimoto (2016), Long-term variation of stratospheric aerosols observed with lidars over Tsukuba, Japan, from 1982 and Lauder, New Zealand, from 1992 to 2015, *J. Geophys. Res. Atmos.*, *121*, 10,283–10,293, doi:10.1002/2016JD025132.

Sanford, T., P. C. Frumhoff, A. Luers, and J. Gulledge (2014), The climate policy narrative for a dangerously warming world, *Nat. Clim. Change*, *4*(3), 164–166, doi:10.1038/nclimate2148.

Santer, B., et al. (2014), Volcanic contribution to decadal changes in tropospheric temperature, *Nat. Geosci.*, *7*, 185–189, doi:10.1038/ngeo2098.

Santer, B. D., et al. (2003), Contributions of anthropogenic and natural forcing to recent tropopause height changes, *Science*, *301*(5632), 479–483, doi:10.1126/science.1084123.

Santer, B. D., et al. (2015), Observed multivariable signals of late 20th and early 21st century volcanic activity, *Geophys. Res. Lett.*, *42*, 500–509, doi:10.1002/2014GL062366.

Sato, M., J. E. Hansen, M. P. McCormick, and J. B. Pollack (1993), Stratospheric aerosol optical depths, 1850–1990, *J. Geophys. Res.*, *98*(D12), 22,987–22,994, doi:10.1029/93JD02553.

Schmidt, A., K. S. Carslaw, G. W. Mann, A. Rap, K. J. Pringle, D. V. Spracklen, M. Wilson, and P. M. Forster (2012), Importance of tropospheric volcanic aerosol for indirect radiative forcing of climate, *Atmos. Chem. Phys.*, *12*(16), 7321–7339, doi:10.5194/acp-12-7321-2012.

Schmidt, A., et al. (2015), Satellite detection, long-range transport, and air quality impacts of volcanic sulfur dioxide from the 2014–2015 flood lava eruption at Bárðarbunga (Iceland), *J. Geophys. Res. Atmos.*, *120*, 9739–9757, doi:10.1002/2015JD023638.

Schmidt, A., et al. (2016), Selective environmental stress from sulphur emitted by continental flood basalt eruptions, *Nat. Geosci.*, *9*, 77–82, doi:10.1038/ngeo2588.

Sherwood, S. C., and N. Nishant (2015), Atmospheric changes through 2012 as shown by iteratively homogenized radiosonde temperature and wind data (IUKv2), *Environ. Res. Lett.*, *10*(5), 54007, doi:10.1088/1748-9326/10/5/054007.

Shindell, D. T., G. A. Schmidt, M. E. Mann, and G. Faluvegi (2004), Dynamic winter climate response to large tropical volcanic eruptions since 1600, *J. Geophys. Res.*, *109*, D05104, doi:10.1029/2003JD004151.

Sigl, M., et al. (2015), Timing and climate forcing of volcanic eruptions for the past 2,500 years, *Nature*, *523*, 543–549.

Simmons, A., P. Poli, D. Dee, P. Berrisford, H. Hersbach, S. Kobayashi, and C. Peubey (2014), Estimating low-frequency variability and trends in atmospheric temperature using ERA-Interim, *Q. J. R. Meteorol. Soc.*, *140*(679), 329–353, doi:10.1002/qj.2317.

Solomon, S., J. S. Daniel, R. R. Neely, J.-P. Vernier, E. G. Dutton, and L. W. Thomason (2011), The persistently variable "background" stratospheric aerosol layer and global climate change, *Science*, *333*(6044), 866–870, doi:10.1126/science.1206027.

Stenchikov, G. L., K. Hamilton, R. J. Stouffer, A. Robock, V. Ramaswamy, B. Santer, and H.-F. Graf (2006), Arctic Oscillation response to volcanic eruptions in the IPCC AR4 climate models, *J. Geophys. Res.*, *111*, D07107, doi:10.1029/2005JD006286.

Stoffel, M., et al. (2015), Estimates of volcanic-induced cooling in the Northern Hemisphere over the past 1,500 years, *Nat. Geosci.*, *8*, 784–788, doi:10.1038/ngeo2526.

Tabazadeh, A., and R. Turco (1993), Stratospheric chlorine injection by volcanic eruptions: HCl scavenging and implications for ozone, *Science*, *260*(5111), 1082–1086, doi:10.1126/science.260.5111.1082.

Taylor, K. E., R. J. Stouffer, and G. A. Meehl (2012), An overview of CMIP5 and the experiment design, *Bull. Am. Meteorol. Soc.*, *93*(4), 485–498, doi:10.1175/bams-d-11-00094.1.

Textor, C., H.-F. Graf, M. Herzog, and J. Oberhuber (2003), Injection of gases into the stratosphere by explosive volcanic eruptions, *J. Geophys. Res.*, *108*(D19), 4606, doi:10.1029/2002JD002987.

Thordarson, T., and S. Self (2003), Atmospheric and environmental effects of the 1783–1784 Laki eruption: A review and reassessment, *J. Geophys. Res.*, *108*(D1), 4011, doi:10.1029/2001JD002042.

Timmreck, C. (2012), Modeling the climatic effects of large explosive volcanic eruptions, *WIREs Clim. Change*, *3*(6), 545–564, doi:10.1002/wcc.192.

Toohey, M., K. Krüger, U. Niemeier, and C. Timmreck (2011), The influence of eruption season on the global aerosol evolution and radiative impact of tropical volcanic eruptions, *Atmos. Chem. Phys.*, *11*(23), 12,351–12,367, doi:10.5194/acp-11-12351-2011.

Toohey, M., K. Krüger, M. Sigl, F. Stordal, and H. Svensen (2016a), Climatic and societal impacts of a volcanic double event at the dawn of the Middle Ages, *Clim. Change*, *136*(3), 401–412, doi:10.1007/s10584-016-1648-7.

Toohey, M., B. Stevens, H. Schmidt, and C. Timmreck (2016b), Easy Volcanic Aerosol (EVA v1.0): An idealized forcing generator for climate simulations, *Geosci. Model Dev. Discuss.*, *2016*, 1–40, doi:10.5194/gmd-2016-83.

Tupper, A., I. Itikarai, M. Richards, F. Prata, S. Carn, and D. Rosenfeld (2007), Facing the challenges of the International Airways Volcano Watch: The 2004/05 eruptions of Manam, Papua New Guinea, *Weather Forecasting*, *22*(1), 175–191, doi:10.1175/waf974.1.

Uppala, S. M., et al. (2005), The ERA-40 re-analysis, *Q. J. R. Meteorol. Soc.*, *131*(612), 2961–3012, doi:10.1256/qj.04.176.

Van Vuuren, D., et al. (2011), The representative concentration pathways: An overview, *Clim. Change*, *109*(1-2), 5–31, doi:10.1007/s10584-011-0148-z.

Vernier, J.-P., L. W. Thomason, T. D. Fairlie, P. Minnis, R. Palikonda, and K. M. Bedka (2013), Comment on "Large volcanic aerosol load in the stratosphere linked to Asian monsoon transport", *Science*, *339*(6120), 647–647, doi:10.1126/science.1227817.

Vernier, J.-P., T. D. Fairlie, T. Deshler, M. Natarajan, T. Knepp, K. Foster, F. G. Wienhold, K. M. Bedka, L. Thomason, and C Trepte (2016), In situ and space-based observations of the Kelud volcanic plume: The persistence of ash in the lower stratosphere, *J. Geophys. Res. Atmos.*, *121*, 11,104–11,118, doi:10.1002/2016JD025344.

Waythomas, C. F., W. E. Scott, S. G. Prejean, D. J. Schneider, P. Izbekov, and C. J. Nye (2010), The 7–8 August 2008 eruption of Kasatochi volcano, central Aleutian Islands, Alaska, *J. Geophys. Res.*, *115*, B00B06, doi:10.1029/2010JB007437.

Wilson, L., R. Sparks, T. Huang, and N. Watkins (1978), The control of volcanic column heights by eruption energetics and dynamics, *J. Geophys. Res.*, *83*, 1829–1836, doi:10.1029/JB083iB04p01829.

Woodhouse, M., A. Hogg, J. Phillips, and R. S. J. Sparks (2013), Interaction between volcanic plumes and wind during the 2010 Eyjafjallajökull eruption, Iceland, *J. Geophys. Res. Solid Earth*, *118*(1), 92–109, doi:10.1029/2012JB009592.

Woodhouse, M. J., A. J. Hogg, J. C. Phillips, and J. C. Rougier (2015), Uncertainty analysis of a model of wind-blown volcanic plumes, *Bull. Volcanol.*, *77*(10), 1–28, doi:10.1007/s00445-015-0959-2.

Woods, A. (1988), The fluid dynamics and thermodynamics of eruption columns, *Bull. Volcanol.*, *50*(3), 169–193, doi:10.1007/BF01079681.

Woods, A. (1993), Moist convection and the injection of volcanic ash into the atmosphere, *J. Geophys. Res.*, *98*(B10), 17,627–17,636, doi:10.1029/93JB00718.

Woods, A. (2010), Turbulent plumes in nature, *Annu. Rev. Fluid Mech.*, *42*, 391–412, doi:10.1146/annurev-fluid-121108-145430.

Woods, A., and K. Wohletz (1991), Dimensions and dynamics of co-ignimbrite eruption columns, *Nature*, *350*(6315), 225–227, doi:10.1038/350225a0.

Wu, T., et al. (2014), An overview of BCC climate system model development and application for climate change studies, *J. Meteorol. Res.*, *28*(1), 34–56, doi:10.1007/s13351-014-3041-7.

Zanchettin, D., et al. (2016), The Model Intercomparison Project on the climatic response to Volcanic forcing (VolMIP): Experimental design and forcing input data, *Geosci. Model Dev. Discuss.*, *2016*, 1–33, doi:10.5194/gmd-2016-68.